


**Crystal fields of lithium rare-earth tetrafluorides and multiplet splitting of the +3 rare-earth ions**Leila Mollabashi and S. Jalali-Asadabadi *Department of Physics, University of Isfahan (UI), Isfahan 81746-73441, Iran*

(Received 15 March 2020; revised 19 June 2020; accepted 30 June 2020; published 14 July 2020)

Construction of an effective Hamiltonian including crystal field parameters (CFPs) by an accurate *ab initio* technique can provide a powerful approach for the measurements of tiny magnetic fields. Here, we first calculate the crystal field parameters (CFPs) of trivalent rare-earth magnetic ions  $R^{3+}$  in lithium rare-earth tetrafluorides  $LiRF_4$  ( $R = Tb, Dy, Ho, Er, Tm,$  and  $Yb$ ) by the density functional theory plus the novel CFP scheme employing open-core treatment and Wannier functions. The behaviors of the real and imaginary parts of the CFPs are studied through the series of compounds. Then, by the calculated CFPs, we find the splittings of the energy levels of the +3 rare-earth ions by constructing an effective Hamiltonian for each case. The multiplet splittings of the +3 rare-earth ions are found to be consistent with those predicted by group theory and Hund's rules apart from some multiplet splitting of the  $Tm^{3+}$  and  $Dy^{3+}$  ions. For the former case, we have compared our theoretical results with the available empirical splittings of the multiplets. However, for the latter case due to the lack of experimental splittings, we have first empirically obtained the splittings of the multiplets employing the available experimental CFPs of the  $LiDyF_3:Dy^{3+}$  single crystal and then compared our empirical data with our *ab initio* theoretical predictions. The deviations of these two ions from the predictions of group theory and Hund's rules are found to be consistent with the experimental data. This validates the results reported and the reliability of the procedures performed to produce them. To simplify the effective Hamiltonian by reducing the number of CFPs, it is sometimes possible to use the  $D_{2d}$  symmetry for some systems having  $S_4$  symmetry. However, by evaluating the matrix elements of the Stevens Hamiltonian term by term appeared in the Stevens CF Hamiltonian, it is shown that the actual  $S_4$  symmetry may provide more reliable results than its successor  $D_{2d}$  symmetry for the systems under study having  $S_4$  symmetry. It can be predicted that this approach can be used for developing and improving sensitive magnetometer devices which, in turn, can play a key role in diverse areas.

DOI: [10.1103/PhysRevB.102.045120](https://doi.org/10.1103/PhysRevB.102.045120)**I. INTRODUCTION**

Electronic structures and magnetic properties of the lanthanide-based compounds may be highly sensitive to their crystalline environments [1]. These features can considerably vary by their crystal electric fields (CEF) [1]. The ability to measure fine and localized magnetic fields plays a key role in developing sensitive magnetometer devices which are important in a variety of areas such as physics, chemistry, material science, and biology [2]. Furthermore, splittings of energy levels of the +3 rare-earth ions due to their crystalline electric fields are of significant importance for the determination of various physical properties such as magnetic, electric, optical, and thermal properties [3]. These properties can be effectively studied by simulating the crystal fields utilizing an appropriate model Hamiltonian for a given system. To this end, the crystal fields exerted on the  $4f$  electrons of the rare earth elements immersed in a crystalline environment can be simulated above the Kondo temperature by an effective atomiclike Hamiltonian, including free ion interaction and single-particle crystal field Hamiltonians [4]. Therefore, the applications of the atomiclike Hamiltonian may be convenient for the study of the physical properties of the rare-earth-based

materials [5]. So far, different theoretical and semiempirical Hamiltonians have been proposed to model the crystal field Hamiltonian, such as point charge, superposition, and overlapping models [6–8]. A review of these models can be found in Ref. [9]. The performance and reliability of these models depend on their constituent terms which, in turn, themselves depend on the crystal field parameters (CFPs) [5]. Therefore, the CFPs play vital roles in the predictions of reliable physical properties and would be determined accurately.

The CFPs can be determined by fitting to the experimental data or empirically by employing a model Hamiltonian or theoretically by performing *ab initio* calculations. The semiempirical models require initial values to estimate the CFPs [10]. Furthermore, the semiempirical models suffer from some difficulties such as selecting a suitable reference system, fitting algorithms, and trapping into the local minima during the fitting process [10]. Moreover, the experimental data used in the semiempirical models may be insufficient to determine all the CFPs (without employing machine learning algorithms) especially when the local symmetry is low. In other words, this is a well-known overparameterization drawback of experimental approaches. Michael Slota *et al.* have presented a multitechnique approach to overcome the latter experimental problem by a combination of various experimental spectroscopic and magnetometric techniques [11]. In addition, since the 1960s it has become clear that not only is CEF a simple electrostatic effect, but CEF also

\*Corresponding author: [sjalali@sci.ui.ac.ir](mailto:sjalali@sci.ui.ac.ir); [saeid.jalali.asadabadi@gmail.com](mailto:saeid.jalali.asadabadi@gmail.com)

includes a complicated quantum mechanics effect. Thus since then, it has become common to perform *ab initio* CEF calculations. So far, CFPs have been calculated for various solid crystals, chemical molecules, and complexes in the last decades [4,12–22]. Most of the *ab initio* CEF calculations have been performed based on the density functional theory (DFT) [23,24] since 1964. Although the regular DFT-based methods have no longer needed the initial values to begin the CEF calculations, they have suffered from their well-known shortcoming in properly treating with the strongly correlated systems [25–29]. Hence, the CFPs predicted by the regular DFT-based methods could be far from the experimental data without special treatments. To overcome the problems of *ab initio* CFP's calculations, recently Pavel Novák and coworkers [4] proposed an approach by expressing the local Hamiltonian in the basis of Wannier functions [30–33] and expanding it in a series of spherical tensor operators using open-core [34–36] treatment. This approach has been successfully applied to calculate CFPs in rare-earth impurities, aluminates, cobaltites, gallates, manganites, and fluorides [4,37–43].

One of the objectives of this work is then to systematically explore the CFPs of trivalent rare earth magnetic ions (the +3 rare-earth) in lithium rare-earth tetrafluorides  $\text{LiRF}_4$  ( $R = \text{Tb, Dy, Ho, Er, Tm, and Yb}$ ) employing the latter advanced *ab initio* CFP approach. Although the CFPs of these compounds have been extensively reported by empirical methods [44–51], the CFP method has not been yet applied to explore the CFPs of  $\text{LiRF}_4$  ( $R = \text{Tb, Dy, Ho, Er, Tm, and Yb}$ ) compounds. Moreover, these complex fluorides  $\text{LiRF}_4$  compounds have shown a variety of fascinating properties. For instance,  $\text{LiYF}_4$  is well known as a host laser doped with trivalent rare earths [52]. Quantum phase transition was reported by Bitko and Rosenbaum [53] in  $\text{LiHoF}_4$  at  $T = 0.5$  K. The transverse susceptibility was measured by Rucker and Pfeleiderer [54] for  $\text{LiHoF}_4$  at a magnetic field where quantum phase transition occurred. Uniaxial dipolar ferromagnetism in  $\text{LiTbF}_4$  and  $\text{LiHoF}_4$  was observed and reported by Beauvillain and coauthors [55]. Kraemer *et al.* established  $\text{LiErF}_4$  as a model dipolar-coupled antiferromagnetic with planar spin-anisotropy and a quantum phase transition performing accurate neutron scattering, specific heat capacity, and magnetic susceptibility measurements [56]. It is well known that NMR of nuclei of Van Vleck paramagnetic systems can be measured at low temperatures.  $\text{LiTmF}_4$  was reported to be a Van Vleck paramagnetic material. Therefore, Abubakrirov *et al.* measured, for the first time, the magnetization of the single crystal at the temperature range of 2–300 K [57]. Babkevich *et al.* [58] measured ac susceptibility, specific heat, and neutron scattering for a dipolar-coupled antiferromagnet  $\text{LiYbF}_4$ . Romanova and coworkers [59] studied temperature and magnetic field dependences of the magnetization of  $\text{LiDyF}_4$  single crystal employing a dc-SQUID magnetometer. Salaün *et al.* measured IR and Raman active modes in  $\text{LiRF}_4$  ( $R = \text{Ho, Er, Tm, Yb}$ ) and  $\text{LiYF}_4/a$  [60].

Furthermore, in this work, we also aim to study all the ground-state crystal field multilevels and its excitation levels by diagonalization of the effective Hamiltonian, including crystal field, spin-orbit coupling, and  $4f$ - $4f$  interactions. The site symmetry of the +3 rare-earth ions in these compounds is  $S_4$  which results in seven independent parameters, where three

(two) of them are real (complex); each complex parameter includes two real parameters, *viz.*  $3 + 2 \times 2 = 7$ . It is worth mentioning that the semiempirical methods could not yield all seven parameters, because of the inadequate experimental data required by the empirical models [4]. To overcome the problem, the  $S_4$  symmetry is commonly approximated by the simpler  $D_{2d}$  symmetry where  $D_{2d}$  requires only five parameters [44,49,61–64]. However, in this work, the actual  $S_4$  symmetry is considered and all of its seven parameters are obtained. It is shown that  $D_{2d}$  is not an appropriate approximation for the compounds in question. Our results, in agreement with the available experimental data, show that the CFP approach can provide a reliable method for further studies of the crystal fields.

To achieve the above goals, here, we have extracted the Wannier functions [30–33] required by the CFP approach from the Bloch's eigenstates calculated by DFT [23,24] employing a full-potential method applying open core [34–36] calculations. By the open core [34–36] treatment, the  $4f$  electrons are made totally localized and thence their hybridizations to the valence states are ignored. To this end, we calculate the electronic structures and project the results into the  $4f$ -electrons subspaces. By this, we first confine the  $4f$  electrons into the core region. Therefore, the  $4f$  electrons involve only the spherical part of the density of  $4f$  electrons and the potential does not have any nonspherical components of  $4f$ -states on the R sites. Thus, self-interaction error and nonphysical interactions of  $4f$  electrons with nonspherical potential produced are prevented to occur [4]. Second, the  $4f$  electrons are released from the core region towards the valence states after determining the relative locations of the  $4f$  states with respect to the other valence states. By this,  $4f$  states are allowed to be hybridized with other valence states. We extract the CFPs by expanding the local Hamiltonians in terms of spherical harmonics. To improve the results, we control the strength of the hybridization by a single  $\Delta$  parameter, as implemented in the CFP scheme [4]. In order to reach the objectives more promptly and straightforwardly as well as to elucidate the key and necessary procedures applied, three appendices are provided where details of various parts of the works performed are represented and accordingly discussed.

## II. THEORETICAL BACKGROUND

The underlying theory of the crystal field is compactly reformulated here in such a way that it can be used to demonstrate how our theoretically calculated Wybourne CFPs are converted to the available experimental and empirical Stevens CFPs. This is necessary for comparison and whence validity of the scheme used and the data reported in this work.

The effective Hamiltonian,  $\hat{H}_{\text{eff}}$ , including the free ion interaction Hamiltonian,  $\hat{H}_A$ , and the single-particle crystal field Hamiltonian,  $\hat{H}_{\text{CF}}$ , is defined as [65]:

$$\hat{H}_{\text{eff}} = \hat{H}_A + \hat{H}_{\text{CF}}, \quad (1)$$

where  $\hat{H}_A$ , consisting of a uniform shift of energy in a central field for  $4f$  electrons and electron-electron as well as spin-orbit interactions, is invariant under rotation and almost independent of the material, see Ref. [65] for details. In contrast to the  $\hat{H}_A$ , the  $\hat{H}_{\text{CF}}$  can be aspherical and thence strongly material

dependent. In the Wybourne notation,  $\hat{H}_{\text{CF}}$  can be written as [66]:

$$\hat{H}_{\text{CF}} = \sum_{k=0}^{k_{\text{max}}} \sum_{q=-k}^k B_q^k \hat{C}_q^k, \quad (2)$$

where  $\hat{C}_q^k$ , as the Racah spherical tensor operators of rank  $k$  operating on  $4f$  electrons, can be expressed in terms of the spherical harmonics  $\hat{Y}_q^k$  as:

$$\hat{C}_q^k = \sqrt{\frac{4\pi}{2k+1}} \hat{Y}_q^k. \quad (3)$$

Regardless of the transition terms of  $\hat{H}_{\text{CF}}$  between states with different angular momenta  $l$ 's, the crystal field parameters  $B_q^k$  can be nonzero in Eq. (2) only if  $k_{\text{max}} = 2l$ . Thus, for our  $4f$  cases with  $l = 3$ ,  $k_{\text{max}}$  is 6. The values of  $q$  are also limited by the site symmetry of the +3 rare-earth ions in Eq. (2). The symmetry of our case is  $S_4$ , see Appendix A. For the  $S_4$  symmetry, the crystal field Hamiltonian can be expanded as follows:

$$\begin{aligned} \hat{H}_{\text{CF}} = & B_0^2 \hat{C}_0^2 + B_0^4 \hat{C}_0^4 + B_0^6 \hat{C}_0^6 \\ & + B_{-4}^4 \hat{C}_{-4}^4 + B_4^4 \hat{C}_4^4 + B_{-4}^6 \hat{C}_{-4}^6 + B_4^6 \hat{C}_4^6. \end{aligned} \quad (4)$$

In general, the  $B_q^k$  ( $\hat{C}_q^k$ ) are complex parameters (operators). The Wybourne  $B_q^k$  parameters are not very suitable for performing comparison with the Stevens parameters, because  $B_q^k$  are complex while the Stevens parameters are real. Fortunately, due to the hermiticity of the  $\hat{H}_{\text{CF}}$  which leads to  $B_{-q}^k = (-1)^q B_q^{k*}$ , the complex  $B_q^k$  parameters can be transformed to a set of real  $\mathbb{B}_q^k$  parameters by defining new  $\hat{\mathbb{C}}_q^k$  operators as [67]:

$$\hat{\mathbb{C}}_{\pm|q|}^k = \begin{cases} \hat{C}_q^k, & \text{if } q = 0, \\ \sqrt{\pm 1} [\hat{C}_{-|q|}^k \pm (-1)^{|q|} \hat{C}_{|q|}^k], & \text{otherwise.} \end{cases} \quad (5)$$

In this case, Eq. (2) can be represented using  $\hat{\mathbb{C}}_q^k$ , as defined in Eq. (5), and the real crystal field parameters  $\mathbb{B}_q^k$ :

$$\hat{H}_{\text{CF}} = \sum_{k=0}^{k_{\text{max}}} \sum_{q=-k}^k \mathbb{B}_q^k \hat{\mathbb{C}}_q^k. \quad (6)$$

Furthermore, if  $q$  in  $B_{-q}^k = (-1)^q B_q^{k*}$  is even, as it is for  $S_4$  symmetry expressed in Eq. (4), there are  $\Re[B_q^k] = \Re[B_{-q}^k]$  and  $\Im[B_q^k] = -\Im[B_{-q}^k]$  relations between the real part  $\Re[B_q^k]$  and imaginary part  $\Im[B_q^k]$  of the complex  $B_q^k$  parameters for every  $k$ . One can also see that  $B_q^k$  are real parameters for  $q = 0$  and every  $k$ , viz.  $B_0^k = (-1)^0 B_0^{k*} = B_0^{k*}$  or similarly  $\Im[B_0^k] = -\Im[B_0^k]$  which gives  $\Im[B_0^k] = 0$ . Consequently, Eq. (4) can be represented by:

$$\begin{aligned} \hat{H}_{\text{CF}} = & B_0^2 \hat{C}_0^2 + B_0^4 \hat{C}_0^4 + B_0^6 \hat{C}_0^6 + \Re[B_4^k] (\hat{C}_4^4 + \hat{C}_{-4}^4) \\ & - i \Im[B_4^k] (\hat{C}_4^4 - \hat{C}_{-4}^4) + \Re[B_4^6] (\hat{C}_4^6 + \hat{C}_{-4}^6) \\ & - i \Im[B_4^6] (\hat{C}_4^6 - \hat{C}_{-4}^6), \end{aligned} \quad (7)$$

By considering Eq. (5), Eq. (7) can be represented in terms of  $\hat{\mathbb{C}}_q^k$ :

$$\begin{aligned} \hat{H}_{\text{CF}} = & B_0^2 \hat{\mathbb{C}}_0^2 + B_0^4 \hat{\mathbb{C}}_0^4 + B_0^6 \hat{\mathbb{C}}_0^6 \\ & + \Re[B_4^k] \hat{\mathbb{C}}_4^4 + \Im[B_4^k] \hat{\mathbb{C}}_{-4}^4 \\ & + \Re[B_4^6] \hat{\mathbb{C}}_4^6 + \Im[B_4^6] \hat{\mathbb{C}}_{-4}^6. \end{aligned} \quad (8)$$

By Eqs. (6) and (8), the complex crystal field parameters  $B_q^k$  can be related to the real crystal field parameters  $\mathbb{B}_q^k$ :

$$\mathbb{B}_q^k = \begin{cases} B_q^k, & \text{if } q = 0, \\ \Re[B_q^k], & \text{if } q > 0, \\ \Im[B_q^k], & \text{if } q < 0. \end{cases} \quad (9)$$

Let us turn our attention to the Stevens notation [68]. The crystal field Hamiltonian in Stevens notation can be written as [1,5,6]:

$$\hat{H}_{\text{CF}} = \sum_{k=0}^{k_{\text{max}}} \sum_{q=-k}^k \mathbb{A}_q^k \langle r^k \rangle \Theta^k(J) \hat{\mathcal{O}}_q^k(J_x, J_y, J_z, J) \quad (10)$$

$$\equiv \sum_{k=0}^{k_{\text{max}}} \sum_{q=-k}^k \tilde{\mathbb{B}}_q^k(J) \hat{\mathcal{O}}_q^k(J_x, J_y, J_z, J), \quad (11)$$

where  $\tilde{\mathbb{B}}_q^k(J) \equiv \mathbb{A}_q^k \langle r^k \rangle \Theta^k(J)$  like  $\mathbb{B}_q^k$  in Eq. (6) are real,  $\mathbb{A}_q^k \langle r^k \rangle$  are the standard notations of the crystal field parameters for  $k$  and  $q$ ,  $\Theta^k(J)$  which depend on the electronic charge distribution are the Stevens factors for the ground multiplets corresponding to the total angular momentum quantum number  $J$  usually denoted by  $\alpha_J$ ,  $\beta_J$  and  $\gamma_J$  for  $k = 2, 4$  and  $6$ , respectively, and  $\hat{\mathcal{O}}_q^k(J_x, J_y, J_z, J)$  are the Stevens equivalent operators [1]. In the Stevens equivalent notation [68],  $x$ ,  $y$ , and  $z$  of the crystal field potential energy were replaced by their equivalent Cartesian components of the total angular momentum operators  $J_x$ ,  $J_y$ , and  $J_z$ , respectively, while, for convenience,  $r^2$  was directly replaced by  $J(J+1)$ , as the eigenvalues of  $J^2$  operator, instead of its equivalent  $J^2$  operator, where  $\hbar$  was assumed to be unity. Thus,  $J$  is just a constant number, as explicitly indicated in the caption of Table VII in the original Stevens' paper [68]. However,  $J_x$ ,  $J_y$ , and  $J_z$  are still operators, e.g., see Eq. (1) in page 211 and the next equations in page 212 of his paper [68]. The expectation values of these operators should be evaluated under  $|4f; \mathbf{L}, \mathbf{S}, \mathbf{J}, J_z\rangle$  or  $|4f; \mathbf{L}, \mathbf{S}, S_z, J_z\rangle$  states, as performed in Tables 2 to 4 of Ref. [68]. Details of the conversion between the Wybourne and Stevens notations are represented elsewhere in Appendix B employing the above formulation.

### III. OBSTACLES AND CFP METHODOLOGY

There are two main problems to reliably predict the CFPs by the density functional theory (DFT) calculations [23,24] for the rare-earth-based compounds under study in this work. The first problem is that the accuracy of the CFPs calculations can considerably depend on the self-interactions of the  $4f$  electrons. This dependency arises from the interactions of the  $4f$  electrons with their own aspherical potentials in the valence states. The second problem which can affect the accuracy of the CFPs calculations is the separation energies of

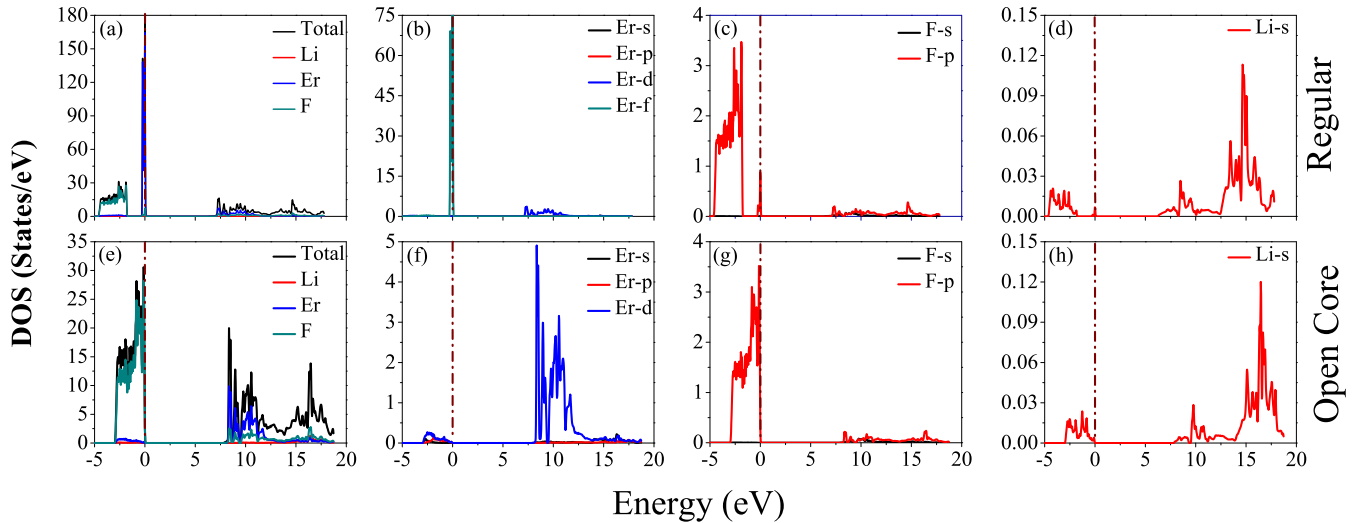


FIG. 1. Total and projected DOSs calculated by PBE-GGA during the *first step* of the CFP scheme employing (a) to (d) regular and (e) to (f) open core treatments for  $\text{LiErF}_4$ . Fermi levels are set to zero, as shown by the vertical dashed lines.

the  $4f$  orbitals of the rare earth ions with respect to the  $2p$  and  $2s$  orbitals of the fluorine ligands. The separation energies can influence the degree of hybridization between the  $4f$  orbitals of the rare earths and the  $2p$  and  $2s$  orbitals of the ligands which in turn can play a key role in the determination of the CFPs. This is a general problem that does not occur only for the CFPs calculations. This lies in the heart of the effective single-particle DFT approach and naturally occurs when it is applied to study the strongly correlated systems employing the standard local density approximation (LDA) [25,69,70] or the generalized gradient approximation (GGA) [71–74]. In this case, it usually fails to well predict the positions of the densities of states (DOSs) in the strongly correlated systems. For such systems, a variety of band correlated schemes such as  $\text{LDA}+U$  [27,75–77] have been proposed. However, the problem becomes more serious, if we note that  $\text{LDA}+U$  cannot be applied to the  $4f$  electrons of our rare-earth-based compounds for the study of their CFPs. Although the position of the  $4f$ -DOS can be adjusted by the  $\text{LDA}+U$  method, it cannot be used here because the number of electrons is fixed in the crystal field optical excitations. On the contrary, the  $\text{LDA}+U$  is specifically designed for the study of those properties, including photoemission or inverse photoemission spectroscopy in which the number of electrons changes.

The above problems can be fixed by the CFP scheme developed by Pavel Novák *et al.* [4] to calculate CFPs. The open-core treatment [4,34–36], which can be specifically used by the augmented plane-waves (APW) based methods such as APW plus local orbital (APW+lo) [78–80], constitutes the *first step* of this scheme, as discussed in Appendix C. By this treatment, the  $4f$  electrons can be transferred from the valence region to the core region and confined there [compare Figs. 1(a) to 1(d) with Figs. 1(e) to 1(h)]. The open core DOSs show that the  $4f$ -Er states are completely absent from the valence region, as should be due to the transportation of the  $4f$  electrons from the valence to the core region, as imposed by the open-core treatment. By such confinement, the  $4f$  electrons cannot (can only) interact with the aspherical

(spherical) component of the electron charge density in the valence (core) region, as can be seen from Figs. 1(e) to 1(h). Therefore, the open-core method can solve the first problem, as it prevents the nonphysical self-interactions of the  $4f$  electrons with themselves.

Furthermore, Figs. 1(f)–1(h) show that the  $d$ -Er-DOS and  $s$ -Li-DOS dominate in the conduction region, while the  $2p$ -F-DOS dominates in the valence region. Therefore, the  $2p$ -F states can be considered as more suitable candidates to be hybridized by the  $4f$ -Er states after releasing the corresponding  $4f$  electrons from the core region towards the valence region, as will be permitted in the following *second step* of the CFP scheme. Similar behaviors to the DOSs of  $\text{LiErF}_4$  sample, not shown here, can be observed for the other  $\text{LiRF}_4$  compounds under study. Hence, the  $2p$ -F states can remain more suitable to hybridize with the  $4f$  electrons of the R ions in the other  $\text{LiRF}_4$  compounds in question.

In the *second step* of the CFP scheme [4], the confined  $4f$  orbitals are released from the core region towards the valence region and allowed to be hybridized with the  $2p$  and  $2s$  orbitals of the fluorine ligands, as discussed above. To solve the second problem, a suitable repulsive orbital dependent potential is properly constructed and applied, see Fig. 2(a). The relative separation energies between the  $4f$  orbitals of the rare-earth ions and the  $2p$  and  $2s$  orbitals of the ligands can be adjusted, as shown in Fig. 2, by an adjustable parameter  $\Delta$ , as expressed by Eq. (12), engineered as the only controllable parameter in the CFP method for this purpose. Consequently, the second problem can be also solved, as the separation energies can be changed and adjusted to control the degree of hybridizations.

In practice, the orbital dependent potential and the adjustable  $\Delta$  parameter in the CFP approach plays a role to mimic the role of  $U$  parameter in the  $\text{LDA}+U$  functional or  $\alpha$  parameter in the hybrid functionals [81–84], though in principle these approaches and their parameters are physically different. Here, by the  $\Delta$  parameter of the CFP scheme, the charge transfer between the rare earth and ligand orbitals

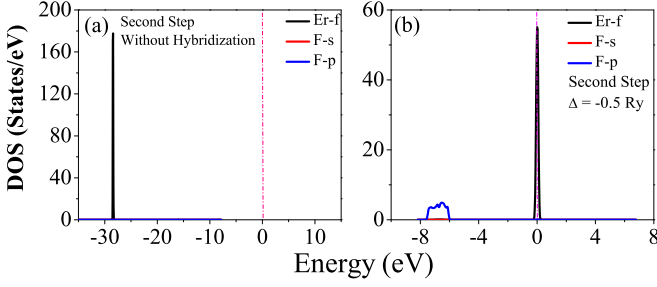


FIG. 2. Projected DOSs calculated by PBE-GGA in the *second step* of the CFP scheme (a) after releasing the  $4f$  electrons from the core and applying an orbital dependent potential to repel the states towards deeper energies with respect to the Fermi surface and (b) imposing an optimized  $\Delta$  parameter to adjust the separation energies and hybridization between  $4f$ -Er and the fluorine states, p-F and s-F, in  $\text{LiErF}_4$ .

can be controlled. In this work, we have optimized the  $\Delta$  parameter for all the cases under study to improve the results, see Fig. 4.

Details of calculations are presented in Appendix C keeping in mind the above problems and the CFP methodology to resolve them. In this work, we will show that the CFP scheme can be a suitable replacement for the inapplicable  $\text{LDA}+U$  to study crystal field effects in the rare-earth based systems, see Sec. IV and its subsections therein.

## IV. RESULTS AND DISCUSSIONS

### A. Effects of hybridization on CFPs

The calculated nonzero independent complex CFPs with  $q \geq 0$  in  $\text{cm}^{-1}$  unit are tabulated in Table I. These CFPs are presented in Wybourne notation, as expressed by Eq. (2) which is simplified to Eq. (4) for the  $S_4$  symmetry. The other dependent CFPs with  $q < 0$  can be straightforwardly obtained from  $B_{-q}^k = (-1)^q B_q^{k*}$  relation, as discussed in Sec. II. The independent CFPs are obtained without and with different hybridization degrees imposed by different  $\Delta$  values following the procedure discussed in Appendix C. From Table I, we notice that by switching on the hybridization from  $|\Delta| = 0.0$  to  $0.2$  Ry, first the absolute values of the CFPs (|CFPs|) decrease compared to when the hybridization switch is off in all the cases with the exception of  $B_0^2$  in  $\text{LiTmF}_4$ . After turning on the hybridization, however, the results then show a reverse behavior so that |CFPs| decrease as the  $|\Delta|$  increases for all the compounds except for  $B_0^2$  in  $\text{LiYbF}_4$  from  $|\Delta| = 0.2$  to  $0.3$  Ry. The size of the CFPs reduction decreases at each step compared to its previous step. This implies that the effects of the hybridizations on the CFPs are gradually reduced by increasing the value of the  $\Delta$  parameter. In Fig. 3, the real and imaginary parts of the CFPs are plotted as functions of the compounds. The CFPs shown in this figure are calculated including the optimized hybridization parameter  $\Delta = -0.5$  Ry in Wybourne notation as formulated in Eq. (4). This figure is presented to show the dependencies of the CFPs on the rare-earths ions in the  $\text{LiRF}_4$  series of the compounds. The results, as shown in Fig. 3, show that the  $B_0^2$  and  $B_0^6$  as well as the imaginary parts of  $B_{-4}^4$  and  $B_{-4}^6$  are all positive, while the  $B_4^4$

TABLE I. Calculated complex independent crystal field parameters ( $B_q^k$  with  $q \geq 0$ ), as expressed by Eq. (4), in unit  $\text{cm}^{-1}$  without and with different hybridization degrees, as imposed by different  $\Delta$  values in Ry, in Wybourne notation for the the  $+3$  rare-earth ions in  $\text{LiRF}_4$  compounds. The  $B_{-q}^k$ , as shown in Fig. 4, can be obtained by  $B_{-q}^k = (-1)^q B_q^{k*}$  and the data presented in this table.

$\text{LiRF}_4$	$\Delta$	$B_0^2$	$B_0^4$	$\Re[B_4^4]$	$\Im[B_4^4]$	$B_0^6$	$\Re[B_4^6]$	$\Im[B_4^6]$
$\text{LiTbF}_4$	0	514	-888	-783	-697	24.2	-781	-576
	-0.2	570	-1114	-1033	-938	34.7	-1013	-739
	-0.3	527	-926	-858	-773	26.8	-811	-597
	-0.4	504	-817	-747	-672	21.7	-700	-510
	-0.5	485	-728	-667	-599	19.0	-616	-448
	-0.6	470	-658	-605	-543	17.3	-553	-400
$\text{LiDyF}_4$	0	413	-891	-770	-630	73.3	-777	-541
	-0.2	466	-1180	-1072	-897	114	-1079	-739
	-0.3	432	-986	-885	-735	86.5	-862	-593
	-0.4	409	-854	-765	-634	71.2	-731	-502
	-0.5	393	-759	-681	-563	61.4	-641	-439
	-0.6	381	-685	-617	-509	54.5	-573	-392
$\text{LiHoF}_4$	0	424	-753	-683	-604	53.7	-663	-459
	-0.2	480	-1048	-1007	-920	80.8	-999	-662
	-0.3	445	-853	-813	-729	57.7	-763	-525
	-0.4	425	-744	-698	-623	48.3	-643	-440
	-0.5	409	-657	-617	-550	42.0	-557	-381
	-0.6	398	-591	-557	-496	37.8	-495	-337
$\text{LiErF}_4$	0	393	-743	-652	-537	64.3	-635	-432
	-0.2	460	-1101	-1022	-877	110	-1037	-674
	-0.3	421	-883	-812	-679	76.6	-772	-526
	-0.4	400	-763	-691	-575	62.3	-644	-433
	-0.5	383	-671	-608	-505	53.2	-554	-372
	-0.6	371	-601	-547	-454	46.9	-489	-328
$\text{LiTmF}_4$	0	329	-349	-338	-310	18.9	-281	-191
	-0.2	229	-1268	-1157	-1348	440	-1913	-563
	-0.3	449	-998	-916	-873	83.5	-956	-571
	-0.4	408	-788	-727	-679	53.1	-698	-440
	-0.5	384	-660	-615	-569	39.3	-559	-363
	-0.6	370	-575	-541	-499	31.8	-474	-313
$\text{LiYbF}_4$	0	359	-579	-570	-523	31.1	-509	-362
	-0.2	374	-926	-948	-1019	98.3	-1014	-543
	-0.3	392	-754	-770	-719	34.2	-694	-482
	-0.4	370	-634	-645	-599	28.3	-561	-391
	-0.5	355	-553	-562	-521	24.9	-477	-333
	-0.6	345	-494	-504	-466	22.8	-419	-292

and the real parts of  $B_{\pm 4}^4$ ,  $B_{\pm 4}^6$  as well as the imaginary parts of  $B_4^4$  and  $B_4^6$  are all negative, for all the compounds. The smallest CFP is  $B_0^6$  in each of the compounds. The  $|\Re[B_{\pm 4}^{4(6)}]|$  CFPs are slightly larger than  $|\Im[B_{\pm 4}^{4(6)}]|$  CFPs for all the compounds. The positive values of  $\Re[B_{-4}^4]$  and  $\Re[B_{-4}^6]$  monotonically but slowly decrease through the compounds apart from  $\Re[B_{-4}^4]$  which jumps up suddenly at  $\text{LiTmF}_4$ . The negative values of  $\Im[B_4^4]$  and  $\Im[B_4^6]$  monotonically but slowly increase through the compounds apart from  $\Im[B_4^4]$  which drops down suddenly at  $\text{LiTmF}_4$  and  $\Im[B_4^6]$  which a little bit falls down at  $\text{LiDyF}_4$ . The similarity in behaviors between negative and positive values confirms the relation  $B_{-q}^k = (-1)^q B_q^{k*}$  due to the hermiticity of the Hamiltonian discussed in Sec. II. Thus, it can be more compactly stated that all the  $\Re[B_{-4}^4]$  and  $\Re[B_{-4}^6]$  as

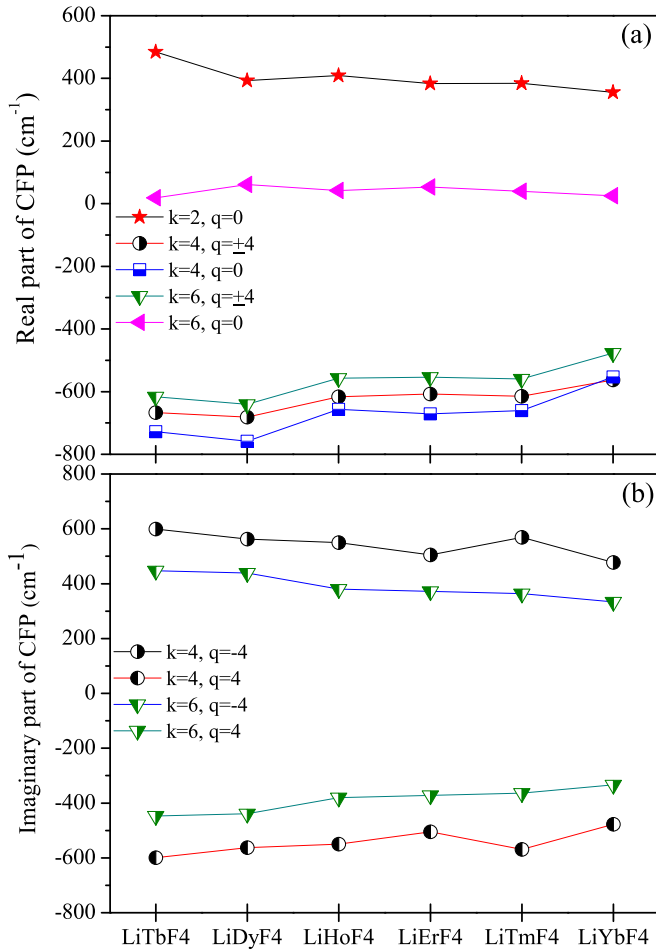


FIG. 3. Dependencies of the (a) real and (b) imaginary parts of the CFPs expressed in Wybourne notation by Eq. (4) on the rare earths R through the series of the  $\text{LiRF}_4$  compounds including hybridization parameter  $\Delta = -0.5$  Ry.

well as  $|\Im[B_4^4]|$  and  $|\Im[B_4^6]|$  decrease through the series of the compounds apart from the aforementioned exceptions. Almost partially the same behaviors and exceptions can be seen in the positive  $B_0^2$ ,  $B_0^4$ , and  $B_0^6$  as well as real parts of the negative  $B_{\pm 4}^6$  and  $B_{\pm 4}^4$ .

### B. Reduction of the number of CFPs

The reduction of the number of CFPs plays a crucial role in the comparison of the theoretical CFPs calculated by the *ab initio* methods with the CFPs extracted from the experimental data by the empirical methods. This returns to the well-known overparameterization shortcoming of the experimental data. This means that for the systems with low symmetry, more experimental data than the available measured data are often needed for determining all the CFPs of the systems by means of the semiempirical models.

In this work, we have calculated all seven CFPs of the crystal field Hamiltonian with  $S_4$  symmetry in the Wybourne notation in  $\text{cm}^{-1}$ , see Table I. However, we have noticed that only five or six of the CFPs have been often experimentally or empirically determined at least for the cases in question. Therefore, in order to compare our calculated CFPs with

the experimental and/or empirical CFPs, we have reduced the number of CFPs. The reduction can be performed by two different approaches. Here, only a summary needed to discuss the results is presented below and the finer details of the reduction procedures are left for Appendix B. We have also noticed that most of the experimental data for the cases under study have been reported in the Stevens notation. Thus, before reducing the number of CFPs, we have converted our Wybourne CFPs and the other few experimental CFPs reported in Wybourne notation to Stevens notation. Due to the similar reason, the Stevens CFPs are converted from  $\text{cm}^{-1}$  to  $\text{meV}$ . For details of the conversion procedures, one may refer to the latter Appendix.

In the first approach, we have used an appropriate unitary Rudowicz transformation [85] in such a way that one of the CFPs of the Hamiltonian is forced to be zero, see Table X. This can be an exact analytical approach for the CEF Hamiltonian considered in this study, namely Eq. (1). To this end, we have determined the rotational angle  $\varphi$  by Eq. (B9) for each case using the CFPs so that one of the CFPs becomes zero in the rotated system. The converted Wybourne CFPs in  $\text{cm}^{-1}$  to the Stevens CFPs in  $\text{meV}$  together with the calculated corresponding rotational angles are tabulated in Table XI. We have used the results presented in this table as an intermediate step (and whence not shown here) for obtaining the final CFPs, as to be presented and discussed subsequently in Sec. IV E. The results presented in this intermediate table show that the value of  $\varphi$  depends on the compound, though the variations of  $\varphi$  are not too much throughout the series. Despite the latter point about the slow variation of the  $\varphi$ , however, since the rotational angle is generally case dependent,  $\varphi$  should be evaluated for each case individually. Furthermore, the results show that the angle  $\varphi$  increases when the optimized  $\Delta = -0.5$  Ry parameter is included. It is worth noticing that no approximation is used in this approach here in this work. This can be considered as an advantage for this method in the absence of external fields, dipolar interactions, Zeeman coupling, and the other interactions because with no approximation the number of CFPs of the  $S_4$  symmetry can be reduced from 7 CFPs to 6 CFPs only by finding the suitable rotational angle  $\varphi$ . In spite of this advantage in the absence of the additional interactions, however, sometimes more reductions in the number of CFPs are needed to be performed. In this case, although the following approach is not an exact method, it may be considered as another alternative to overcome the lack of sufficient experimental data.

In the second approach, the main symmetry  $S_4$  is approximated by an auxiliary symmetry  $D_{2d}$  for the cases considered here. The symmetry group  $D_{2d}$  can be a suitable successor for this purpose because it is closer to and more symmetric than the primary group  $S_4$ . In fact,  $S_4$  is a subgroup of  $D_{2d}$ . Two terms with  $q < 0$  in the Stevens CEF Hamiltonian for the  $S_4$  symmetry, as written in Eq. (11), are not included in the corresponding Stevens CEF Hamiltonian for the  $D_{2d}$  symmetry, as expressed in Eq. (B10). It is like the  $\mathbb{B}_{-4}^{4(6)}$  parameters are eliminated from the effective Hamiltonian by considering  $D_{2d}$  instead of the actual subgroup  $S_4$ . This is due to the higher symmetry of  $D_{2d}$  than  $S_4$ . Thus, the number of CFPs of the auxiliary symmetry group is less than that of the original symmetry group. The number of CFPs

is five for  $D_{2d}$ , which can be more suitable when there are not enough experimental data to determine all 7 CFPs of the  $S_4$  or 6 CFPs of the rotated  $S_4$  used in the first approach. Although this is an approximating method, it can be used for estimating the CFPs in the absence of enough experimental data. The accuracy of this approximation is subsequently verified in Sec. IV C for the compounds under question.

Finally, it would be noticed that even the first approach cannot be considered as an exact method in the presence of an external magnetic field, dipolar coupling, Zeeman effect, and so on. This is so because in the presence of additional interactions the  $\varphi$  angle may not be straightforwardly determined. However, there are no such limitations for the CFP scheme.

### C. Matrix elements of Stevens Hamiltonian term by term

It can be seen from Table XI that the  $\tilde{\mathbb{B}}_0^2$  is the largest parameter in every compound. From this incomplete observation, at first glance, one may conjecture that the  $\tilde{\mathbb{B}}_0^2$  parameter can more significantly affect the physical properties derived from the effective Hamiltonian than the other parameters. In order to verify this conjecture, we analytically evaluate matrix elements individually appearing in  $\mathcal{H}_{CF}$  which is defined to be the matrix elements of the Stevens Hamiltonian operator, *viz.*  $\mathcal{H}_{CF} = \langle J, M_J | \hat{H}_{CF}(J_+, J_-, J_z, J) | J, M_J \rangle$  where the Stevens Hamiltonian operator therein  $\hat{H}_{CF}$  is given by Eq. (11). To this end, first, the matrix elements of the Stevens equivalent operators  $\mathcal{O}_q^k$  are obtained, where  $\mathcal{O}_q^k$  stands for  $\langle J, M_J | \hat{O}_q^k(J_+, J_-, J_z, J) | J, M_J \rangle$ . In evaluating  $\mathcal{O}_q^k$  for every given  $q, k, J$ , and  $M_J$ , the values of  $M_J$  are selected such that the corresponding matrix elements  $\mathcal{O}_q^k$  do not vanish, see Table II. To obtain the matrix elements  $\mathcal{O}_q^k$ , we have utilized the Stevens equivalent operators  $\hat{O}_q^k(J_+, J_-, J_z, J)$  as tabulated in Table IX in terms of  $J_+, J_-, J_z$  operators and  $X \equiv J(J+1)$  eigenvalues. To act  $J_+, J_-, J_z$  operators on the  $|J, M_J\rangle$  states of the systems, we have used the corresponding Clebsch-Gordan coefficients and assumed  $\hbar$  to be unity. According to the Stevens equivalent notation, however, the  $X \equiv J(J+1)$  term, appearing in the Stevens operators  $\hat{O}_q^k$  listed in Table IX, is treated only as a constant eigenvalue of the  $J^2$  operator, see also the notes on the  $J_+, J_-, J_z$  operators and  $J(J+1)$  eigenvalue after Eq. (11) in Sec. II. Our derived matrix elements with positive  $q$  are validated by Refs. [6,86]. The validity of our derived matrix elements with negative  $q$  are verified by Refs. [87,88]. Second, we have multiplied the obtained  $\mathcal{O}_q^k$  by  $\tilde{\mathbb{B}}_q^k$ . The latter  $\tilde{\mathbb{B}}_q^k$  CFPs are taken from the intermediate Table XI, where all the 7 CFPs are presented. Ultimately, the matrix elements for each term of the Stevens CEF Hamiltonian, namely  $\tilde{\mathbb{B}}_q^k \mathcal{O}_q^k$ , are presented in Table II.

The results show that only the matrix elements  $|\tilde{\mathbb{B}}_0^6 \mathcal{O}_0^6|$  are approximately one order of magnitude smaller than the other matrix elements for all the cases apart from  $\text{LiTbF}_4:\text{Tb}^{3+}$ . For the latter case,  $|\tilde{\mathbb{B}}_0^6 \mathcal{O}_0^6|$  is two orders of magnitude smaller than the other matrix elements, see Table II. However, the results of this table also show that the matrix elements  $|\tilde{\mathbb{B}}_0^2 \mathcal{O}_0^2|$  are almost of comparable order with those of  $|\tilde{\mathbb{B}}_0^4 \mathcal{O}_0^4|$  and  $|\tilde{\mathbb{B}}_{\pm 4}^{4(6)} \mathcal{O}_{\pm 4}^{4(6)}|$ . This shows that the conjecture may not be generally correct. Indeed, both of the counterparts of the product of  $\tilde{\mathbb{B}}_q^k \mathcal{O}_q^k$  included in the CEF Stevens Hamiltonian

should be considered and not merely one of them, namely,  $\tilde{\mathbb{B}}_q^k$  counterpart as imperfectly considered in the above conjecture.

Moreover, the results, as tabulated in Table II, also show that the matrix elements  $|\tilde{\mathbb{B}}_{-4}^4 \mathcal{O}_{-4}^4|$  are of the same order of magnitude with those of  $|\tilde{\mathbb{B}}_{-4}^4 \mathcal{O}_{-4}^4|$ . Our results show that  $|\tilde{\mathbb{B}}_{-4}^6 \mathcal{O}_{-4}^6|$  are a little bit smaller than the other matrix elements only for the  $\text{LiTbF}_4:\text{Tb}^{3+}$  case. For the other cases,  $|\tilde{\mathbb{B}}_{-4}^6 \mathcal{O}_{-4}^6|$  are comparable with the other matrix elements. This shows that ignoring the former matrix elements with  $q < 0$  compared to the latter matrix elements having  $q > 0$  may not be completely correct, because at least they are in the same order. Therefore, it can be cautiously stated that the actual  $S_4$  symmetry may be more reliable than the approximated  $D_{2d}$  symmetry for the  $\text{LiRF}_4$  ( $R = \text{Tb, Dy, Ho, Er, Tm, and Yb}$ ) systems having  $S_4$  symmetry.

From the discussions presented in Secs. IV B and IV C, it would be seen that the *ab initio* CFP scheme used here can be considered as a modern powerful technique. It is due to the fact that the CFP scheme can reproduce all the crystal field parameters of the systems under study with no need to rotate the system by an angle or approximate the symmetry group of the system by a simpler or a more symmetric successor group of the main group.

### D. Tuning of hybridization parameter

As discussed in Sec. III, one of the obstacles for the study of the CEF in the rare-earth-based compounds using an *ab initio* approach is that LDA+ $U$  method [27,75–77] cannot be applied. To overcome this problem, we implement a recent new theoretical-computational method, *i.e.*, the so-called CFP scheme [4]. In this method, there is a parameter  $\Delta$  which can be used for tuning the degree of hybridization. Such tuning is arbitrary and can be performed at the end of the second step of this method. All the steps of the CFP scheme [4], as performed in this work, are discussed in detail elsewhere in Appendix C. Here, we only concentrate on tuning the degree of hybridization between the  $4f$  orbitals of the rare earths and the  $2p$  and  $2s$  orbitals of the ligands. Even though such tuning is optional, we show that it can play a crucial role in the accuracy of the CFPs calculated for the compounds under question by this scheme.

To tune the hybridization parameter, we first estimate the  $\Delta$  parameter as follows [4,39,41]:

$$|\Delta| \approx \min[E_{\text{exc}}(4f^{n\pm 1}, N \mp 1) - E_{\text{gro}}(4f^n, N)], \quad (12)$$

where  $\min$  stands for the minimum of,  $N = N_{\text{val}} - n$  is the total number of valence electrons ( $N_{\text{val}}$ ) excluded the number of  $f$  electrons ( $n$ ),  $E_{\text{gro}}(4f^n, N)$  is the total ground state energy, and  $E_{\text{exc}}(4f^{n\pm 1}, N \mp 1)$  is the total excited state energy for which the upper (lower) sign shows that one of the  $N_{\text{val}}$  electrons is added to (subtracted from) the  $4f$  orbital. In contrast to the LDA+ $U$  scheme, it is worth it to recall that in the CFP scheme the total number of valence electrons remains unchanged after excitation, *i.e.*,  $n \pm 1 + N \mp 1 = n + N = N_{\text{val}}$ , compared to that of the ground state, *i.e.*,  $n + N = N_{\text{val}}$ , which is required for the CFPs calculations. This shows that the CFP scheme can provide an appropriate applicable

TABLE II. Matrix elements  $\tilde{\mathbb{B}}_q^k \mathcal{O}_q^k$  appearing in the matrix elements of the Stevens Hamiltonian  $\mathcal{H}_{CF}$  for the +3 rare-earth ions in the LiRF<sub>4</sub> series of the compounds, where  $\mathcal{O}_q^k = \langle J, M_J | \hat{\mathcal{O}}_q^k(J_+, J_-, J_z, J) | J, M_J \rangle$  and  $\mathcal{H}_{CF} = \langle J, M_J | \hat{H}_{CF}(J_+, J_-, J_z, J) | J, M_J \rangle$ . The Stevens Hamiltonian operator  $\hat{H}_{CF}$  is expressed in Eq. (11) and the  $\tilde{\mathbb{B}}_q^k$  parameters are given in Table XI. Stevens equivalent operators  $\hat{\mathcal{O}}_q^k(J_+, J_-, J_z, J)$  in terms of  $J_+, J_-, J_z$  operators and  $X \equiv J(J+1)$  eigenvalue are given in Table IX.

$R^{3+}$	$(J, M_J    J, M_J)$	$\tilde{\mathbb{B}}_0^2 \mathcal{O}_0^2$	$\tilde{\mathbb{B}}_0^4 \mathcal{O}_0^4$	$\tilde{\mathbb{B}}_0^6 \mathcal{O}_0^6$	$(J, M_J    J, M_J)$	$\tilde{\mathbb{B}}_4^4 \mathcal{O}_4^4$	$ \tilde{\mathbb{B}}_{-4}^4 \mathcal{O}_{-4}^4 $	$\tilde{\mathbb{B}}_4^6 \mathcal{O}_4^6$	$ \tilde{\mathbb{B}}_{-4}^6 \mathcal{O}_{-4}^6 $
Tb <sup>3+</sup>	$(6, \pm 6    6, \pm 6)$	-20.1	-8.20	-0.03	$(6, 2    6, -2)$	-8.90	7.99	-1.82	1.32
	$(6, \pm 5    6, \pm 5)$	-10.3	4.97	0.07	$(6, \pm 3    6, \mp 1)$	-8.45	7.58	-1.20	0.87
	$(6, \pm 4    6, \pm 4)$	-1.82	7.95	-0.01	$(6, \pm 4    6, 0)$	-7.14	6.40	0.32	0.24
	$(6, \pm 3    6, \pm 3)$	4.56	4.47	-0.05	$(6, \pm 5    6, \pm 1)$	-5.17	4.03	1.85	1.34
	$(6, \pm 2    6, \pm 2)$	9.12	-0.91	-0.03	$(6, \pm 6    6, \pm 2)$	-2.83	2.54	2.25	1.63
	$(6, \pm 1    6, \pm 1)$	11.9	-5.30	0.02					
	$(6, 0    6, 0)$	12.8	-6.96	-0.05					
Dy <sup>3+</sup>	$(15/2, \pm 15/2    15/2, \pm 15/2)$	-16.3	11.4	0.44	$(15/2, \pm 5/2    15/2, \mp 3/2)$	10.2	8.43	6.20	4.24
	$(15/2, \pm 13/2    15/2, \pm 3/2)$	-9.77	-3.80	-0.80	$(15/2, \pm 7/2    15/2, \mp 1/2)$	9.54	7.88	3.47	2.38
	$(15/2, \pm 11/2    15/2, \pm 11/2)$	-4.18	-9.23	-0.27	$(15/2, \pm 9/2    15/2, \pm 1/2)$	8.26	6.82	-1.00	0.69
	$(15/2, \pm 9/2    15/2, \pm 9/2)$	0.465	-8.39	0.40	$(15/2, \pm 11/2    15/2, \pm 3/2)$	6.50	5.37	-5.52	3.78
	$(15/2, \pm 7/2    15/2, \pm 7/2)$	4.185	-4.22	0.59	$(15/2, \pm 13/2    15/2, \pm 5/2)$	4.44	3.68	-8.08	5.53
	$(15/2, \pm 5/2    15/2, \pm 5/2)$	6.98	0.96	0.31	$(15/2, \pm 15/2    15/2, \pm 7/2)$	2.32	1.91	-7.03	4.8
	$(15/2, \pm 3/2    15/2, \pm 3/2)$	8.83	5.39	-0.17					
	$(15/2, \pm 1/2    15/2, \pm 1/2)$	9.76	7.89	-0.51					
Ho <sup>3+</sup>	$(8, \pm 8    8, \pm 8)$	-6.76	7.40	-0.61	$(8, 2    8, -2)$	6.70	5.07	-10.4	7.14
	$(8, \pm 7    8, \pm 7)$	-4.22	-1.85	0.99	$(8, \pm 3    8, \mp 1)$	6.51	5.80	-8.44	5.77
	$(8, \pm 6    8, \pm 6)$	-2.03	-5.55	0.45	$(8, \pm 4    8, 0)$	5.94	5.29	3.08	2.11
	$(8, \pm 5    8, \pm 5)$	-0.17	-5.55	-0.38	$(8, \pm 5    8, \pm 1)$	5.05	4.50	3.93	2.69
	$(8, \pm 4    8, \pm 4)$	1.35	-3.42	-0.75	$(8, \pm 6    8, \pm 2)$	3.91	3.48	10.1	6.94
	$(\pm 3, 8    \pm 3, 8)$	2.53	-0.43	-0.54	$(8, \pm 6    8, \pm 2)$	2.64	2.35	10.1	8.89
	$(8, \pm 2    8, \pm 2)$	3.38	2.42	-0.01	$(8, \pm 8    8, \pm 4)$	1.36	1.21	10.59	7.25
	$(8, \pm 1    8, \pm 1)$	3.88	4.41	0.50					
	$(8, 0    8, 0)$	4.05	5.13	0.70					
Er <sup>3+</sup>	$(15/2, \pm 15/2    15/2, \pm 15/2)$	6.33	-7.57	0.77	$(15/2, \pm 5/2    15/2, \mp 3/2)$	-6.83	5.68	-10.7	7.19
	$(15/2, \pm 13/2    15/2, \pm 13/2)$	3.80	2.52	-1.38	$(15/2, \pm 7/2    15/2, \mp 1/2)$	-6.38	5.31	6.01	4.03
	$(15/2, \pm 11/2    15/2, \pm 11/2)$	1.63	6.13	-0.46	$(15/2, \pm 9/2    15/2, \pm 1)$	-5.53	4.60	-1.73	1.16
	$(15/2, \pm 9/2    15/2, \pm 9/2)$	-0.18	5.57	0.70	$(15/2, \pm 11/2    15/2, \pm 3/2)$	-4.35	3.62	-9.55	6.41
	$(15/2, \pm 7/2    15/2, \pm 7/2)$	-1.63	2.80	1.03	$(15/2, \pm 13/2    15/2, \pm 5/2)$	-2.97	2.47	-14.0	9.39
	$(15/2, \pm 5/2    15/2, \pm 5/2)$	-2.71	-0.64	0.53	$(15/2, \pm 15/2    15/2, \pm 7/2)$	-1.56	1.29	-12.2	8.17
	$(15/2, \pm 3/2    15/2, \pm 3/2)$	-3.44	-3.58	-0.30					
	$(15/2, \pm 1/2    15/2, \pm 1/2)$	-3.80	-5.24	-0.89					
Tm <sup>3+</sup>	$(6, \pm 6    6, \pm 6)$	15.8	-9.92	-0.28	$(6, 2    6, -2)$	-10.9	10.1	-8.25	3.54
	$(6, \pm 5    6, \pm 5)$	7.92	6.01	0.71	$(6, \pm 3    6, \mp 1)$	-10.4	9.56	-5.44	2.33
	$(6, \pm 4    6, \pm 4)$	1.44	9.62	-0.10	$(6, \pm 4    6, 0)$	-8.76	8.08	1.47	0.63
	$(6, \pm 3    6, \pm 3)$	-3.6	5.41	-0.56	$(6, \pm 5    6, \pm 1)$	-6.34	5.85	8.38	3.59
	$(6, \pm 2    6, \pm 2)$	-7.2	-1.10	-0.28	$(6, \pm 6    6, \pm 2)$	-3.47	3.20	10.2	4.37
	$(6, \pm 1    6, \pm 1)$	-9.36	-6.41	0.26					
	$(6, 0    6, 0)$	-10.1	-8.42	0.52					
Yb <sup>3+</sup>	$(7/2, \pm 7/2    7/2, \pm 7/2)$	14.68	6.22	0.04	$(7/2, \pm 5/2    7/2, \mp 3/2)$	13.1	12.2	4.47	3.12
	$(7/2, \pm 5/2    7/2, \pm 5/2)$	2.10	-11.54	-0.18	$(7/2, \pm 7/2    7/2, \mp 1/2)$	8.95	8.31	-6.54	4.57
	$(7/2, \pm 3/2    7/2, \pm 3/2)$	-6.29	-2.66	0.32					
	$(7/2, \pm 1/2    7/2, \pm 1/2)$	-10.5	7.99	-0.18					

approach for the CFP prediction compared to the inapplicable LDA+*U* approach, since in the latter approach the  $N_{\text{val}}$  varies.

After estimating an initial value for the  $\Delta$ , we then elaborate to improve it as much as possible by varying the  $\Delta$  parameter and comparing our results with the reliable experimental values to reach the desired results. Since the  $\Delta$  parameter can be case dependent, we perform this procedure to optimize the  $\Delta$  parameters for all the compounds under study individually as follows, see Table III.

The absolute values of the  $\Delta$  parameters are estimated by Eq. (12) and found that they are larger than 0.2 for all the cases. The data given in Tables III and IV show that the CFPs are in better agreement with the experimental and/or empirical results, if the hybridization  $\Delta$  parameter lies in the  $[-0.6, -0.3 \text{ Ry}]$  interval for Tb<sup>3+</sup> ion, in the  $[-0.6, -0.4 \text{ Ry}]$  interval for Dy<sup>3+</sup>, Ho<sup>3+</sup>, and Er<sup>3+</sup> ions, in the  $[-0.5, -0.5 \text{ Ry}]$  interval for Tm<sup>3+</sup>, and in the 0.0 plus  $[-0.5, -0.4 \text{ Ry}]$  interval for Yb<sup>3+</sup> ion. To find an optimized value for the



TABLE III. Transformed crystal field parameters (CFPs) as expressed by Eq. (B7) in meV for different degrees of hybridization  $\Delta$  parameters for the +3 rare-earth in LiRF<sub>4</sub> compounds in Stevens notation.

LiRF <sub>4</sub>	$\Delta$	$10^3 \times \tilde{B}_0^2$	$10^3 \times \tilde{B}_0^4$	$10^3 \times \tilde{B}_4^4$	$10^3 \times \tilde{B}_{-4}^4$	$10^6 \times \tilde{B}_0^6$	$10^6 \times \tilde{B}_4^6$	$10^6 \times  \tilde{B}_{-4}^6 $
LiTbF <sub>4</sub>	0	-322	-1.68	-16.6	0.00	-0.210	94.3	8.69
	-0.2	-357	-2.11	-22.2	0.00	-0.302	122	13.1
	-0.3	-330	-1.76	-18.3	0.00	-0.233	97.8	9.69
	-0.4	-316	-1.55	-16.0	0.00	-0.188	84.0	8.68
	-0.5	-304	-1.38	-14.2	0.00	-0.165	73.9	7.63
	-0.6	-294	-1.25	-12.9	0.00	-0.150	66.2	6.99
LiDyF <sub>4</sub>	0	-163	0.817	7.64	0.00	0.588	-85.0	6.60
	-0.2	-183	1.08	10.7	0.00	0.914	-117	11.3
	-0.3	-170	0.904	8.83	0.00	0.693	-93.8	8.51
	-0.4	-161	0.783	7.58	0.00	0.571	-79.5	7.66
	-0.5	-155	0.696	6.78	0.00	0.492	-69.7	6.31
	-0.6	-150	0.628	6.14	0.00	0.437	-62.3	5.61
LiHoF <sub>4</sub>	0	-58.4	0.389	3.93	0.00	-0.538	90.1	10.7
	-0.2	-66.1	0.541	5.89	0.00	-0.810	133	20.8
	-0.3	-61.3	0.440	4.72	0.00	-0.578	103	13.3
	-0.4	-58.5	0.384	4.04	0.00	-0.484	87.0	11.2
	-0.5	-56.3	0.339	3.57	0.00	-0.421	75.3	9.71
	-0.6	-54.8	0.305	3.22	0.00	-0.378	66.8	8.73
LiErF <sub>4</sub>	0	61.8	-0.511	-4.86	0.00	1.03	-138	12.6
	-0.2	72.4	-0.758	-7.79	0.00	01.76	-221	30.7
	-0.3	66.3	-0.608	-6.10	0.00	1.23	-167	16.5
	-0.4	63.0	-0.525	-5.18	0.00	0.999	-139	14.2
	-0.5	60.3	-0.462	-4.55	0.00	0.853	-120	12.2
	-0.6	58.4	-0.414	-4.09	0.00	0.752	-105	10.8
LiTmF <sub>4</sub>	0	206	-0.883	-9.71	0.00	-0.821	164	24.0
	-0.2	143	-3.21	-37.6	0.00	-19.7 1	816	529
	-0.3	281	-2.25	-26.8	0.00	-3.63	530	120
	-0.4	255	-1.99	-21.0	0.00	-2.31	395	75.8
	-0.5	240	-1.67	-17.7	0.00	-1.71	320	55.2
	-0.6	232	-1.45	-15.6	0.00	-1.38	264	35.6
LiYbF <sub>4</sub>	0	707	15.5	174	0.00	35.7	-7981	997
	-0.2	736	24.9	313	0.00	113	-14014	4797
	-0.3	771	20.2	237	0.00	39.2	-10768	1563
	-0.4	728	17.0	198	0.00	32.5	-8720	1227
	-0.5	699	14.8	172	0.00	28.5	-7420	1031
	-0.6	679	13.3	154	0.00	26.1	-6514	902

$\Delta$  parameter, however, the consistency of the splittings with the experimental data should be also considered. From the calculated splittings of the energy levels, as shown in Fig. 4, it can be seen that the sensitivity of the splittings to the  $\Delta$  parameter for Yb<sup>3+</sup> ion is less than that for Tm<sup>3+</sup> ion but more than that for Tb<sup>3+</sup>, Dy<sup>3+</sup>, Ho<sup>3+</sup>, and Er<sup>3+</sup> ions, especially in higher multiplets. Furthermore, the splittings calculated by  $\Delta = -0.5$  Ry show good agreement with the experimental data for Tb<sup>3+</sup>, Ho<sup>3+</sup>, Er<sup>3+</sup>, Tm<sup>3+</sup>, and Yb<sup>3+</sup> ions, see Fig. 4. Moreover, the splittings are also consistent with the experimental data even in the absence of hybridization for the Yb<sup>3+</sup> ion.

Taking all the above points deduced from Tables III and IV as well as Fig. 4 into consideration, we conclude that the most suitable hybridization parameter can be  $\Delta = -0.5$  Ry for all the compounds in this study. Therefore, in the subsequent sections, the optimized value of  $-0.5$  Ry is imposed for the hybridization  $\Delta$  parameter for obtaining the final results presented in this work.

### E. Comparison to experimental CFPs

The CFPs of the +3 rare-earth ions in the LiRF<sub>4</sub> series of the compounds are transformed using the Czeslaw Rudowicz transformation relations employing the first approach discussed in Sec. IV B, for more details see also Appendix B. The results are represented in Table IV excluding and including the optimized hybridization  $\Delta$  parameters for all the compounds in the Stevens notation as expressed by Eq. (B7). As can be seen from Table IV, all the  $\tilde{B}_{-4}^4$  CFPs are zero, as expected from the first approach discussed in Sec. IV B. This shows the CFPs are correctly transformed which in turn implies that rotational angles  $\varphi$  are properly calculated. The experimental and/or empirical data are also given for comparison in Table IV.

Our calculated CFPs for the Tm<sup>3+</sup> ion in its own home-crystal LiTmF<sub>4</sub> are found in agreement with the experimental results reported by Jenssen *et al.* [98] for Tm<sup>3+</sup> ion in the so-called YLF single crystal, i.e., LiYF<sub>4</sub>, see

TABLE IV. Transformed crystal field parameters (CFPs) of the +3 rare-earth in meV without and with the optimized hybridization  $\Delta$  parameters for  $\text{LiRF}_4$  compounds in Stevens notation as expressed by Eq. (B7) together with the experimental and empirical results. The results calculated in the present work are denoted by \*. The transformations are performed by considering the Stevens CFPs and the case dependent  $\varphi$  rotational angle, as tabulated in Table XI, as well as the transformation relations represented in Table X.

$\text{LiRF}_4$	$\Delta$	$10^3 \times \mathbb{B}_0^2$	$10^3 \times \mathbb{B}_0^4$	$10^3 \times \mathbb{B}_4^4$	$10^3 \times \mathbb{B}_{-4}^4$	$10^6 \times \mathbb{B}_0^6$	$10^6 \times \mathbb{B}_4^6$	$10^6 \times  \mathbb{B}_{-4}^6 $	Ref.
$\text{LiTbF}_4$	0.0	-322	-1.68	-16.6	0.00	-0.210	94.3	8.69	*
	-0.5	-304	-1.38	-14.2	0.00	-0.165	73.9	7.63	*
		-279	-1.44	-17.8	0.00	-0.0347	74.2	59.4	[89]
		-304	-0.843	-18.4	0.00	-0.747	90.9	31.0	[61]
		-250	-1.53	-16.4	0.00	0.278	69.0	21.1	[90]
		-384	-1.65	-17.7	0.00	0.356	71.8	0.00	[64] <sup>a</sup>
$\text{LiDyF}_4$	0.0	-163	0.817	7.64	0.00	0.588	-85.0	6.60	*
	-0.5	-155	0.696	6.78	0.00	0.492	-69.7	6.31	*
		-130	0.646	7.19	0.00	-0.565	-54.8	8.34	[96]
		-126	0.609	7.25	0.00	-0.590	-55.4	6.27	[59]
		-142	0.676	7.22	0.00	-0.280	-63.0	0.00	[64] <sup>b</sup>
$\text{LiHoF}_4$	0.0	-58.4	0.389	3.93	0.00	-0.538	90.1	10.7	*
	-0.5	-56.3	0.339	3.57	0.00	-0.421	75.3	9.71	*
		-64.8	0.426	4.54	0.00	0.100	85.6	16.9	[49]
		-52.2	0.323	3.59	0.00	0.522	68.5	0.00	[44]
		-73.6	0.478	4.69	0.00	0.100	86.1	11.8	[61]
		-60.0	0.350	3.60	0.00	0.400	70.0	9.80	[97]
		-57.9	0.309	3.51	0.00	0.540	63.1	17.1	[47]
-53.2	0.325	3.63	0.00	0.331	77.3	0.00	[64] <sup>c</sup>		
$\text{LiErF}_4$	0.0	61.8	-0.511	-4.86	0.00	1.03	-138	12.6	*
	-0.5	60.3	-0.462	-4.55	0.00	0.853	-120	12.2	*
		67.8	-0.678	-6.83	0.00	-0.080	-133	24.3	[49]
		49.2	-0.390	-4.14	0.00	-0.899	-92.6	0.00	[44]
		76.3	-0.568	-6.37	0.00	-1.72	-132	23.4	[61]
		47.8	-0.53	-5.39	0.00	-0.961	-120	0.00	[62]
		60.2	-0.120	-4.33	0.00	-1.90	-85.0	22.7	[56]
		58.1	-0.536	-5.53	0.00	-0.0063	-106	23.8	[47]
51.2	-0.515	-5.84	0.00	-0.305	-114	0.00	[64] <sup>d</sup>		
$\text{LiTmF}_4$	0.0	206	-0.883	-9.71	0.00	-0.821	164	24.0	*
	-0.5	240	-1.67	-17.7	0.00	-1.71	320	55.2	*
		225	-1.54	-17.9	0.00	7.52	307	0.00	[98] <sup>e</sup>
		230	-1.81	-19.4	0.00	2.78	300	57.6	[91]
		231	-1.82	-17.9	0.00	2.82	302	0.0236	[57]
		212	-1.59	-19.3	0.00	1.69	285	0.00	[64] <sup>f</sup>
$\text{LiYbF}_4$	0.0	707	15.5	174	0.00	35.7	-7981	997	*
	-0.5	699	14.8	172	0.00	28.5	-7420	1031	*
		737	16.5	176	0.00	-18.4	-4070	0.00	[95] <sup>g</sup>
		720	16.4	177	0.00	-18.4	-5150	0.00	[63] <sup>h</sup>
		457	7.75	196	0.00	0.00	-9780	0.00	[47]
		878	15.0	189	0.00	-26.4	-6693	0.00	[64] <sup>i</sup>

<sup>a</sup> $\text{LiYF}_4:\text{Tb}$ .

<sup>b</sup> $\text{LiYF}_4:\text{Dy}$ .

<sup>c</sup> $\text{LiYF}_4:\text{Ho}$ .

<sup>d</sup> $\text{LiYF}_4:\text{Er}$ .

<sup>e</sup> $\text{LiYF}_4:\text{Tm}$ .

<sup>f</sup> $\text{LiYF}_4:\text{Tm}$ .

<sup>g</sup> $\text{LiYF}_4:\text{Yb}$ .

<sup>h</sup> $\text{LiYF}_4:\text{Yb}$ .

<sup>i</sup> $\text{LiYF}_4:\text{Yb}$ .

Table IV. They [98] first analyzed the corresponding absorption and fluorescence spectra and then determined the energy levels of the ground state  $4f^{12}$  electronic configuration at temperatures between 5 to 77 K using the electric-dipole selection rules in the  $D_{2d}$  symmetry to consider

some of the missing lines and the relative intensities of the observed lines. Eventually, they [98] extracted the CFPs by fitting the Hamiltonian to the corresponding experimental data and allowing us to vary the parameters of the Hamiltonian to reach a least-root-mean-square deviation of

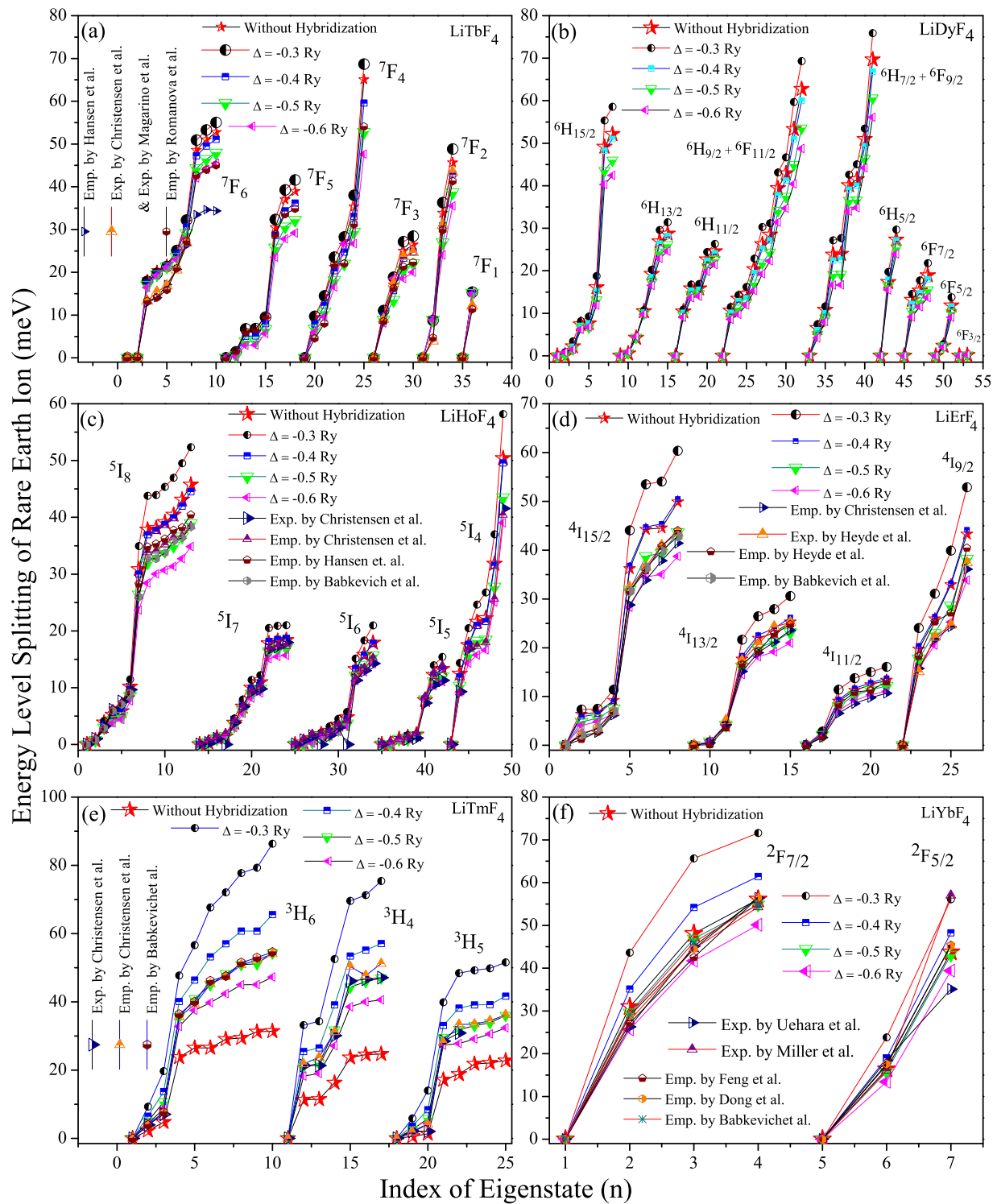


FIG. 4. Splittings of energy levels of the +3 rare-earth ions Li relative to the lowest energies of the multiplets calculated by considering different degrees of hybridizations imposing different  $\Delta$  parameters versus indexes of eigenstates  $n$  for (a)  $\text{LiTbF}_4$ , (b)  $\text{LiDyF}_4$ , (c)  $\text{LiHoF}_4$ , (d)  $\text{LiErF}_4$ , (e)  $\text{LiTmF}_4$ , and (f)  $\text{LiYbF}_4$  compounds compared to the experimental data taken from (a) Refs. [48,49,89,90], (c) Refs. [44,47,49], (d) Refs. [44,47,62], (e) Refs. [47,91], and (f) Refs. [47,63,92–95].

$16.9 \text{ cm}^{-1}$  between the calculated and experimental energy levels.

Similarly, our results are found comparable with the results reported by Cheng Jun *et al.* [64]. They [64], using a parametric effective Hamiltonian and employing

the f-shell program package, analyzed the energy level parameters by the least-squares linear and/or second-order polynomial fitting to the experimental energy level data sets across the lanthanide ions in the YLF single crystal.

These consistencies with the above experimental data [64,98] show that although, for example, the crystal LiTmF<sub>4</sub> (LiTbF<sub>4</sub>) used in present work differs from the host crystal YLF used in Ref. [98] (Ref. [64]) for the Tm<sup>3+</sup> (Tb<sup>3+</sup>) ion, the results are comparable to each other. This might show that the crystalline environment of the host crystal LiYF<sub>4</sub> for the guest ion Tm<sup>3+</sup> (Tb<sup>3+</sup>) may not be probably very different from that of the LiTmF<sub>4</sub> (LiTbF<sub>4</sub>) for the Tm<sup>3+</sup> (Tb<sup>3+</sup>) ion.

For most of the other compounds, as included in Table IV, almost the same consistency can be seen. The other pieces of evidence would be also seen taking the Yb case into account. Dong *et al.* [95] and Feng *et al.* [63] calculated CFPs using optical spectra reported by Miller *et al.* [93] and Uehara *et al.* [92] for LiYF<sub>4</sub>:Yb<sup>3+</sup> with D<sub>2d</sub> site symmetry. These reconfirm that the YLF might be a suitable fluoride laser host for the +3 rare-earth ions when the +3 rare-earth ions occupy the Y site.

In addition to the above agreement with the experimental measurements taking the +3 rare-earth as the guest ions in the host crystal YLF, the calculated CFPs are also compared and found consistent with the available experimental data measured for the +3 rare-earth ions in their own home-crystal LiRF<sub>4</sub> [44,47,49,56,57,59,61,61,62,89–91,96,97], see Table IV. At the end of this subsection, it is worth pointing out that we have obtained the whole set of seven crystal field parameters, a “new” agreement with experimental and empirical data, and we have also provided a comprehensive comparison to results in the literature.

### E. Electronic configuration

Electronic configurations of the ions play a key role like a toolbox for the splitting discussion presented in the next subsection. Therefore, electronic configurations, to be readily accessible, are tabulated in Table V using the Hund’s laws for the ground and excited states of the +3 rare-earth ions in the LiRF<sub>4</sub> compounds, since we frequently refer to this table in Sec. IV G. This table includes the +3 rare-earth ions, numbers of 4*f* electrons (N<sub>4*f*</sub>), total spin angular momenta (S), total orbital angular momenta (L), total angular momenta ( $J = L + S$ ), term values ( $^{2S+1}X_J$ ), and irreducible representations (Γ) of the ions in the LiRF<sub>4</sub> compounds. The numbers of the 4*f* electrons are obtained after removing three electrons from the neutral atoms. For example, the number of 13 4*f* electrons for the Yb<sup>3+</sup> ion is obtained by ionizing the Yb:[Xe]4f<sup>14</sup>6s<sup>2</sup> neutral atom to the Yb<sup>3+</sup>:[Xe]4f<sup>13</sup>6s<sup>0</sup> positively charged ion, as indicated in the last or before the last row of the second column of Table V. The values of S, L, and J are determined in agreement with the values reported in Ref. [47]. The term values are then determined employing the latter S, L, and J. For instance, the  $^{2S+1}X_J$  for Yb<sup>3+</sup> are obtained to be  $^2F_{5/2}$  and  $^2F_{7/2}$ , where X ≡ F symbol stands for L = 3, and 2S + 1 = 2 × 1/2 + 1 = 2, as well as 5/2 = |3 − 1/2| = |L − S| ≤ J ≤ |L + S| = |3 + 1/2| = 7/2 ⇒ J = 5/2 and 7/2. All the S, L, J, and term values are similarly determined using the above procedure for the other ions indicated in Table V.

### G. Comparison to experimental spectra

The splittings of the energy levels are calculated for all the compounds using a variety of Δ parameters. The effects of

TABLE V. Electronic configurations of the ground and excited states of the +3 rare-earth ions in the LiRF<sub>4</sub>, including the +3 rare-earth ions, numbers of 4*f* electrons (N<sub>4*f*</sub>), total spin angular momentum numbers (S), total orbital angular momentum numbers (L), total angular momentum numbers ( $|L - S| \leq J \leq |L + S|$ ), term values ( $^{2S+1}X_J$ ), and irreducible representations (Γ).

R <sup>3+</sup>	N <sub>4<i>f</i></sub>	S	L	J	$^{2S+1}X_J$	Γ
Tb <sup>3+</sup>	8	3	3	6	$^7F_6$	3Γ <sub>1</sub> + 4Γ <sub>2</sub> + 3Γ <sub>3,4</sub>
				5	$^7F_5$	3Γ <sub>1</sub> + 2Γ <sub>2</sub> + 3Γ <sub>3,4</sub>
				4	$^7F_4$	3Γ <sub>1</sub> + 2Γ <sub>2</sub> + 2Γ <sub>3,4</sub>
				3	$^7F_3$	Γ <sub>1</sub> + 2Γ <sub>2</sub> + 2Γ <sub>3,4</sub>
				2	$^7F_2$	Γ <sub>1</sub> + 2Γ <sub>2</sub> + Γ <sub>3,4</sub>
				1	$^7F_1$	Γ <sub>1</sub> + Γ <sub>3,4</sub>
				0	$^7F_0$	Γ <sub>1</sub>
Dy <sup>3+</sup>	9	5/2	5	15/2	$^6H_{15/2}$	4Γ <sub>5,6</sub> + 4Γ <sub>7,8</sub>
				13/2	$^6H_{13/2}$	3Γ <sub>5,6</sub> + 4Γ <sub>7,8</sub>
				11/2	$^6H_{11/2}$	3Γ <sub>5,6</sub> + 3Γ <sub>7,8</sub>
				9/2	$^6H_{9/2}$	3Γ <sub>5,6</sub> + 2Γ <sub>7,8</sub>
				7/2	$^6H_{7/2}$	2Γ <sub>5,6</sub> + 2Γ <sub>7,8</sub>
				5/2	$^6H_{5/2}$	Γ <sub>5,6</sub> + 2Γ <sub>7,8</sub>
				11/2	$^6F_{11/2}$	3Γ <sub>5,6</sub> + 3Γ <sub>7,8</sub>
				9/2	$^6F_{9/2}$	3Γ <sub>5,6</sub> + 2Γ <sub>7,8</sub>
				7/2	$^6F_{7/2}$	2Γ <sub>5,6</sub> + 2Γ <sub>7,8</sub>
				5/2	$^6F_{5/2}$	Γ <sub>5,6</sub> + 2Γ <sub>7,8</sub>
				3/2	$^6F_{3/2}$	Γ <sub>5,6</sub> + Γ <sub>7,8</sub>
				1/2	$^6F_{1/2}$	Γ <sub>7,8</sub>
				Ho <sup>3+</sup>	10	2
7	$^5I_7$	3Γ <sub>1</sub> + 4Γ <sub>2</sub> + 4Γ <sub>3,4</sub>				
6	$^5I_6$	3Γ <sub>1</sub> + 4Γ <sub>2</sub> + 3Γ <sub>3,4</sub>				
5	$^5I_5$	3Γ <sub>1</sub> + 2Γ <sub>2</sub> + 3Γ <sub>3,4</sub>				
4	$^5I_4$	3Γ <sub>1</sub> + 2Γ <sub>2</sub> + 2Γ <sub>3,4</sub>				
15/2	$^4I_{15/2}$	4Γ <sub>5,6</sub> + 4Γ <sub>7,8</sub>				
Er <sup>3+</sup>	11	3/2	6	13/2	$^4I_{13/2}$	3Γ <sub>5,6</sub> + 4Γ <sub>7,8</sub>
				11/2	$^4I_{11/2}$	3Γ <sub>5,6</sub> + 3Γ <sub>7,8</sub>
				9/2	$^4I_{9/2}$	3Γ <sub>5,6</sub> + 2Γ <sub>7,8</sub>
				6	$^3H_6$	3Γ <sub>1</sub> + 4Γ <sub>2</sub> + 3Γ <sub>3,4</sub>
Tm <sup>3+</sup>	12	1	5	5	$^3H_5$	3Γ <sub>1</sub> + 2Γ <sub>2</sub> + 3Γ <sub>3,4</sub>
				4	$^3H_4$	3Γ <sub>1</sub> + 2Γ <sub>2</sub> + 2Γ <sub>3,4</sub>
				7/2	$^2F_{7/2}$	2Γ <sub>5,6</sub> + 2Γ <sub>7,8</sub>
Yb <sup>3+</sup>	13	1/2	3	5/2	$^2F_{5/2}$	Γ <sub>5,6</sub> + 2Γ <sub>7,8</sub>

the Δ parameters on the splittings of the energy levels can be observed in Fig. 4, as discussed in Sec. IV D. However, here for the current spectral discussion, we would only concentrate on the results calculated by the optimized parameter Δ = −0.5 Ry, as shown in Figs. 6 and 7. Therefore, the results obtained from the other (unoptimized) delta values are not included any more here in Figs. 6 and 7. Instead, rather than the removed unoptimized results, we have included (in Figs. 6 and 7) the other important features which can provide useful insights for the spectral applications, as to be discussed below in parts “Energy Gap” and “Singlets & Doublets.” In addition to our pure theoretical prediction, we have also included our empirical results for the Dy<sup>3+</sup> ion in LiDyF<sub>4</sub>, as to be discussed subsequently in part “LiDyF<sub>4</sub>” and shown in Fig. 6(a).

The LiRF<sub>4</sub> (R = Tb, Dy, Ho, Er, Tm, and Yb) series of the compounds are divided into Kramers and non-Kramers classes based on the J quantum numbers of their rare-earth

ions, as determined in Table V: the Kramers class contains  $\text{LiDyF}_4$ ,  $\text{LiErF}_4$ , and  $\text{LiYbF}_4$  crystals, and the non-Kramers class consists of  $\text{LiTbF}_4$ ,  $\text{LiHoF}_4$ , and  $\text{LiTmF}_4$  crystals. In the Kramers class, the total angular momentum numbers  $J$  of the +3 rare-earth ions are half-integers, while they are integers in the non-Kramers class, see Table V. In the Kramers category, the +3 rare-earth ions having half-integer  $J$  total angular quantum numbers and odd parities satisfy the Kramers' theorem, which implies that all the states can be divided into doubly degenerate  $\Gamma_{5,6}$  and  $\Gamma_{7,8}$  states. In the non-Kramers category, the energy levels of the +3 rare-earth ions with integer  $J$  total angular quantum numbers and even parities can be divided into nondegenerate  $\Gamma_1$  and  $\Gamma_2$  states for even  $M_J$  and a doubly degenerate  $\Gamma_{3,4}$  state for odd  $M_J$ . The splittings of the energy levels versus indexes of eigenstates together with the available experimental data [44,47,62,63,92–95] are shown in Fig. 6 for the Kramers class. The splittings of the non-Kramers class are also compared with the corresponding experimental data [44,47–49,89–91] in Fig. 7. In Figs. 6 and 7, the splittings are measured with respect to the lowest energies of the multiplets which are shifted to the zero level, as to be discussed in part “Energy Shift.”

The energy levels can be split by both the spin-orbit coupling (SOC) and the crystal electric field (CEF). The number of splittings and irreducible representations can be qualitatively predicted by group theory for a specified symmetry. However, much more elaborations should be performed to calculate the eigenvalues quantitatively in the presence of the SOC and CEF. Therefore, in this work, we quantitatively calculate the splittings for all the compounds in question. We notice that the strength of the spin-orbit (SO) interaction is much larger than that of CEF interaction in the rare-earth-based compounds. Thus, following the procedure of the perturbation theory, we first include the larger term, i.e., SOC Hamiltonian, and find the splitting only due to the SOC in the absence of CEF.

To clarify what we have performed for all the compounds in this work, let us begin the splitting discussion with the  $\text{LiYbF}_4$  compound as a first sample among the series of our selected compounds, see Fig. 5. The  $\text{LiYbF}_4$  is considered for the following discussion because the number of multiplets of the  $\text{Yb}^{3+}$  ion and their splittings are smaller and thence its discussion can be presented more promptly than the other ions, see Table V, Figs. 5 and 6(c) as well as part “Energy Shift.”

### 1. $\text{LiYbF}_4$

For this case, as discussed in Sec. IV F, the term value is  ${}^2F$  for the ground state of the  $\text{Yb}^{3+}$  ion in the free space, i.e., in the absence of both the SOC and CEF, see Table V. The eigenvalue of the  ${}^2F$  state is 14-fold degenerate, see Fig. 5 where the degeneracy degree is shown as (14) right below the energy level; viz. for the free  $\text{Yb}^{3+}$  ion in the absence of SO interaction the number of degeneracy is obtained as  $(2L + 1)(2S + 1) = (2 \times 3 + 1)(2 \times 1/2 + 1) = 7 \times 2 = 14$ . Now, let us first turn on the SO interaction. We observe that the 14-fold degenerate  ${}^2F$  ground state splits into the ground  ${}^2F_{7/2}$  and excited  ${}^2F_{5/2}$  states in the presence of the SOC but still in the absence of the CEF, as shown in Fig. 5.

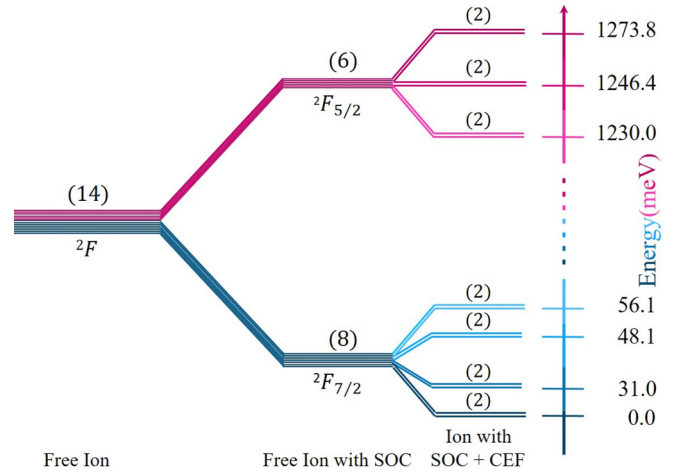


FIG. 5. Energy level splitting of the free  $\text{Yb}^{3+}$  ion by the spin-orbit interaction and then followed by the electric field of the  $\text{LiYbF}_4$  crystal. The degeneracy degrees are shown by the numbers enclosed in parentheses for each energy level. The values of the energy level splittings in meV calculated in this work with taking no hybridization into account are quantitatively represented nearby the vertical energy axis; see also Fig. 6(c).

This is in agreement with the prediction of group theory, see Table V. The separation energy between the ground  ${}^2F_{7/2}$  and the excited  ${}^2F_{5/2}$  states, not indicated here, is of the order of eV. The  ${}^2F_{7/2}$  and  ${}^2F_{5/2}$  states remain still eightfold and sixfold degenerate, respectively, viz.  $1 \times 8 + 1 \times 6 = 8 + 6 = 14$ , where  $8 = 2J + 1 = 2 \times 7/2 + 1$  and  $6 = 2J + 1 = 2 \times 5/2 + 1$ , see Fig. 5. Then, let us add the second smaller CEF term to find further splittings due to this term. In this case, the  ${}^2F_{5/2}$  and  ${}^2F_{7/2}$  states are split into three and four levels, respectively, by the SO plus CEF interactions, see Fig. 5. Although the number of degeneracy is reduced by SOC + CEF, each of the levels of the  ${}^2F_{7/2}$  and  ${}^2F_{5/2}$  states still remains twofold degenerate, viz.  $4 \times 2 + 3 \times 2 = 8 + 6 = 14$ , see Fig. 5 and Table V. This means that all the calculated states are doublet. This is not only consistent with group theory prediction but also with the Kramers' theorem for half-integer  $J$ . This time, the separation energy between the states split by the SOC + CEF is of the order of meV which is three orders of magnitudes smaller than that split by SOC only. The energy level splittings are quantitatively calculated without considering hybridization  $\Delta$  parameter for the  $\text{Yb}^{3+}$  ion in the  $\text{LiYbF}_4$  crystal. The values of the energy level splittings in meV are quantitatively represented nearby the vertical energy axis shown in Fig. 5.

### 2. Energy shift

Although the above traditional presentation for the +3 rare-earth in the  $\text{LiYbF}_4$ , as shown in Fig. 5, is more physically understandable, it needs a lot of space for presenting the results of all the cases. The space problem will be more serious when more data would be reported, including the splittings calculated by various  $\Delta$  parameters and/or available experimental and empirical data as well as spectral information. Therefore, to fix the space problem, the splittings of the energy levels calculated by the optimized hybridization

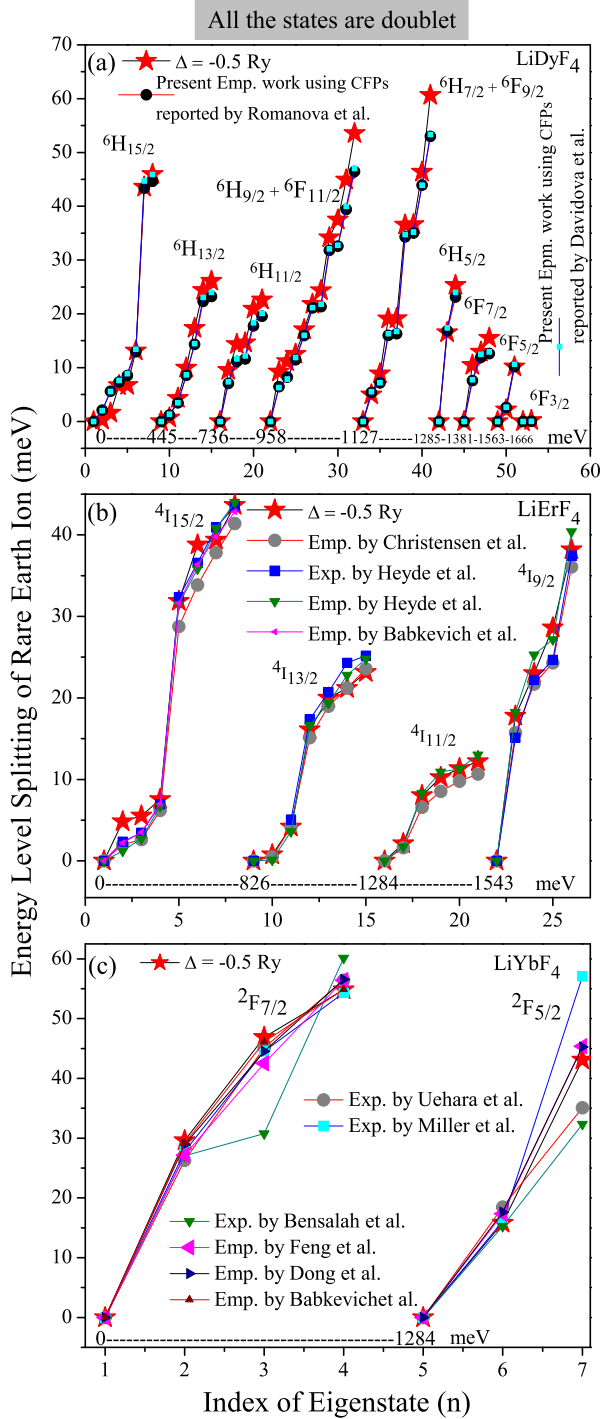


FIG. 6. Splittings of energy levels of the +3 rare-earth ions calculated by imposing optimized  $\Delta (= -0.5 \text{ Ry})$  parameter relative to the lowest energies of the multiplets versus indexes of eigenstates  $n$  for the Kramers compounds (a)  $\text{LiDyF}_4$ , (b)  $\text{LiErF}_4$ , and (c)  $\text{LiYbF}_4$  compared to the experimental data taken from (b) Refs. [44,47,62], and (c) Refs. [47,63,92–95]. The lowest energy of each multiplet in meV calculated by imposing optimized  $\Delta (= -0.5 \text{ Ry})$  is indicated at the bottom (starting point) of each multiplet. In addition to our calculated data theoretically, our calculated data empirically using the CFPs reported in Refs. [59] and [96] for the  $\text{Dy}^{3+}$  ion in  $\text{LiDyF}_4$  are also included for comparison due to the lack of empirical data for this case. All the states shown in the whole of this figure are doubly degenerate.

parameter along with the experimental and/or empirical data are all more compactly presented for all the compounds under study in Figs. 4 and 7 as well as 6. To this end, the energy levels are also rescaled by setting the starting points of the energy levels to zero for the ground and excited states in Figs. 4 and 7 as well as 6. These energy shifts are performed, because the energy levels separated by the SOC are three orders of magnitude larger than those by separated CEF, and thereby they cannot be illustrated on the same scale in a single figure.

### 3. Energy gap

Although the space problem is managed by the above strategy, the energy gap between the adjacent multiplets is still missed in Fig. 4 which includes a lot of unoptimized results. However, the gap between the highest energy level of a multiplet and the lowest energy level of the adjacent (higher) multiplet is quite an important feature, particularly here in Sec. IV G for understanding the relevance of multiplet mixing. Therefore, to deduce this crucial quantity from represented spectra, the lowest energy of each multiplet is indicated at the bottom (starting point) of each multiplet individually only in Figs. 6 and 7 after excluding the unoptimized results which should be included in Fig. 4.

### 4. Singlets and doublets

Another important feature that is again missing in Fig. 4 is the possibility to distinguish singlets from doublets. Although the sequence of the (singlet, doublet) structure can be obtained for each multiplet of each compound from the data given in this paper, it would be helpful, if it can be deduced illustratively from the presented spectra, as well. However, this vital feature is not included in Fig. 4 containing many unoptimized results. Therefore, here, in order to illustrate the sequence of the structure so that it can be straightforwardly seen from the spectra, we have used *solid symbols* for doublets and *empty symbols* for singlets in Figs. 6 and 7 which are made free from the unoptimized results. Furthermore, we have also distinguished them by indicating  $\mathbb{D}$  besides the *solid symbols* for doublets and  $\mathbb{S}$  besides the *empty symbols* for singlets in these figures.

### 5. $\text{LiDyF}_4$

For this case, all the calculated states are doubly degenerate in agreement with the Kramers' theorem. It is observed that our calculated  ${}^6\text{H}_{9/2}$  multiplet is mixed to  ${}^6\text{F}_{11/2}$  multiplet resulting in a mixed multiplet of  ${}^6\text{H}_{9/2} + {}^6\text{F}_{11/2}$ , see fourth excited multiplet in Fig. 6(a). Furthermore, the  ${}^6\text{H}_{7/2}$  multiplet is also mixed to  ${}^6\text{F}_{9/2}$  multiplet leading to another mixed multiplet as  ${}^6\text{H}_{7/2} + {}^6\text{F}_{9/2}$ , see fifth excited multiplet in see Fig. 6(a). These observations clearly contradict the prediction of group theory and Hund's rules [compare Fig. 6(a) with Table V]. Interestingly, these predicted mixed multiplets,  ${}^6\text{H}_{9/2} + {}^6\text{F}_{11/2}$  and  ${}^6\text{H}_{7/2} + {}^6\text{F}_{9/2}$ , are found consistent with the experimental measurements reported in Tables 1 and 2 as well as Fig. 2 of Ref. [99] for the dysprosium ion in  $\text{KPB}_2\text{Cl}_5:\text{Dy}^{3+}$  and  $\text{YLF}:\text{Dy}^{3+}$ , where YLF stands for  $\text{LiYF}_4$ . From this consistency, one may conjecture that the CFP scheme can satisfactorily predict extraordinary cases,

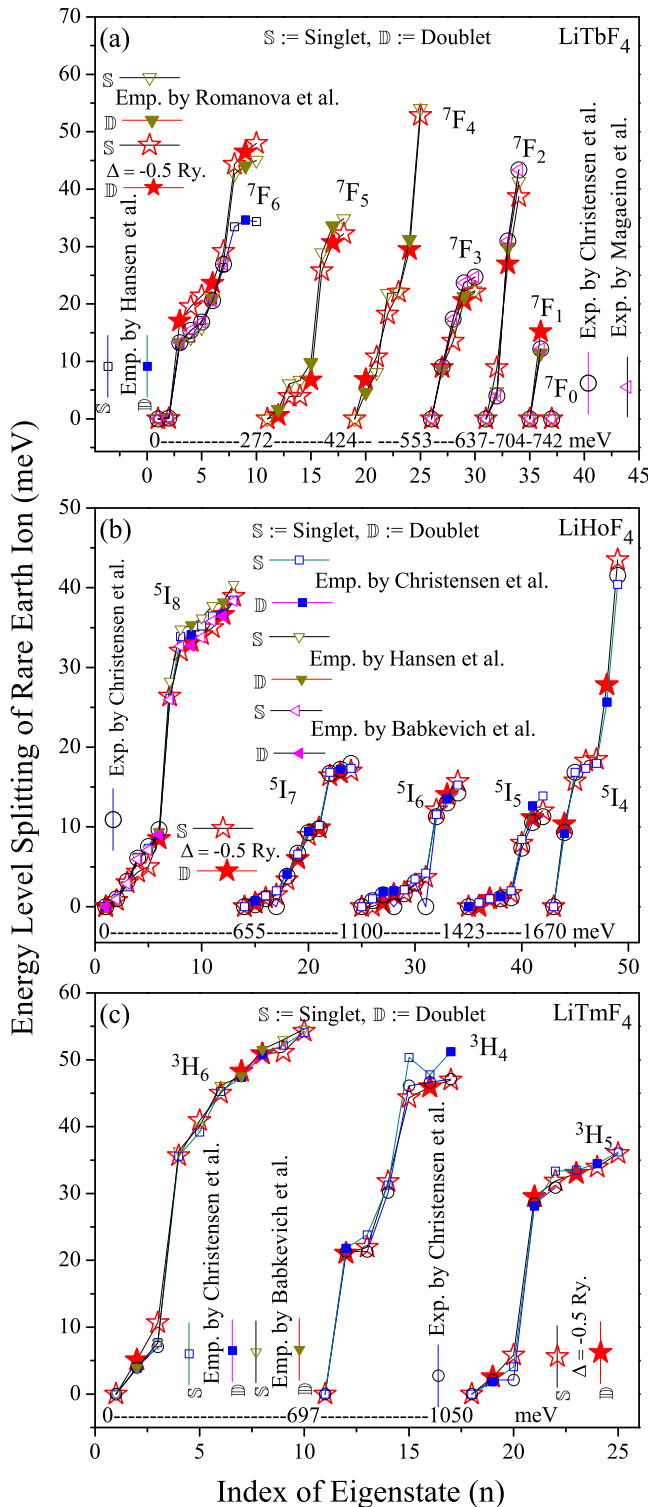


FIG. 7. Splittings of energy levels of the +3 rare-earth ions calculated by imposing optimized  $\Delta (= -0.5 \text{ Ry})$  parameter relative to the lowest energies of the multiplets versus indexes of eigenstates  $n$  for the non-Kramers compounds (a)  $\text{LiTbF}_4$ , (b)  $\text{LiHoF}_4$ , and (c)  $\text{LiTmF}_4$  compared to the experimental data taken from (a) Refs. [48,49,89,90], (b) Refs. [44,47,49], and (c) Refs. [47,91]. The lowest energy of each multiplet in meV calculated by imposing optimized  $\Delta (= -0.5 \text{ Ry})$  is indicated at the bottom (starting point) of each multiplet. Singlet (doublet) states are shown by empty (solid) symbols with the indicators of S (D).

as well. However, it should be noted that although the point group symmetry for  $\text{Dy}^{3+}$  ion in  $\text{YLF:Dy}^{3+}$  is also  $S_4$ , this is not the case for  $\text{Dy}^{3+}$  ion substituting  $\text{K}^+$  or  $\text{Pb}^{2+}$  ions in  $\text{KPb}_2\text{Cl}_5$ . Therefore, an explicit conclusion inferred from the comparison of  $\text{LiDyF}_4:\text{Dy}^{3+}$  and  $\text{KPb}_2\text{Cl}_5:\text{Dy}^{3+}$  requires more elaborations than that of  $\text{LiDyF}_4:\text{Dy}^{3+}$  and  $\text{YLF:Dy}^{3+}$ .

Anyway, since the above conclusion is solely inferred based on the experimental data reported for the other Dy-based materials [99], for sure in addition to our pure *ab initio* theoretical results, we have also empirically extracted the multiplets of the  $\text{Dy}^{3+}$  ion in the  $\text{LiDyF}_4$  from two different sets of experimental CFPs, as well. The first set of the experimental CFPs is taken from Ref. [59] reported by Romanova *et al.*, and the second set is taken from Ref. [96] reported by Davidova *et al.* To this end, we have solved the eigenvalue problem for the effective Hamiltonian expressed in Eq. (1) using the RECFP code [4] as a modified version of the LANTHANIDE code [100] implemented into the CFP code [4]. Our obtained empirical splittings are also included in Fig. 6(a) for comparison. The comparison of our *ab initio* theoretical splittings predicted by the CFP scheme with our empirical splittings extracted from the two sets of the experimental data [59,96] show that all the splittings are in agreement with each other, see Fig. 6(a). This assures that the deviation from the prediction of group theory is not only consistent with our theoretical prediction but also it is in complete accord with our empirical predictions and whence with the experimental data [59,96].

## 6. $\text{LiTbF}_4$

Let us turn now our attention to the splittings of  $\text{Tb}^{3+}$  ion in the  $\text{LiTbF}_4$  as one of our selected non-Kramers system. The splittings of the energy levels of the  $\text{Tb}^{3+}$  ion in  $\text{LiTbF}_4$  compound, as shown in Fig. 7(a), shows that the  ${}^7F_6$  multiplet splits into three doublet and seven singlet states. The next  ${}^7F_5$  multiplet splits into three doublet and five singlet states. The other multiplets including  ${}^7F_4$ ,  ${}^7F_3$ ,  ${}^7F_2$ ,  ${}^7F_1$ , and  ${}^7F_0$  are also shown in Fig. 7(a). These results are in agreement with the experimental data reported in Refs. [48,49,89,90]. The ground state term value of the free  $\text{Tb}^{3+}$  ion is  ${}^7F$  in the absence of the SOC and CEF, see Table V. The eigenvalue of the  ${}^6F$  state is 49-fold degenerate; *viz.*  $(2L+1)(2S+1) = (2 \times 3 + 1)(2 \times 3 + 1) = 7 \times 7 = 49$ . The 49-fold degenerate  ${}^7F$  state of  $\text{Tb}^{3+}$  ion splits by SO interaction into seven multiplets. The seven multiplets of  $\text{Tb}^{3+}$  ion are  ${}^7F_6$ ,  ${}^7F_5$ ,  ${}^7F_4$ ,  ${}^7F_3$ ,  ${}^7F_2$ ,  ${}^7F_1$ , and  ${}^7F_0$ , see Table V. The multiplet  ${}^7F_6$  is 13-fold degenerate; *viz.*  $2J+1 = 2 \times 6 + 1 = 13$ . The next five multiplets,  ${}^7F_5$ ,  ${}^7F_4$ ,  ${}^7F_3$ ,  ${}^7F_2$ ,  ${}^7F_1$ , are 11-fold, 9-fold, 7-fold, 5-fold, 3-fold degenerate, respectively. The last multiplet  ${}^7F_0$  is nondegenerate (nd). The sum of the degeneracies of the multiplets in the presence of the SOC is equal to the degeneracy of the free ion in the absence of the SOC; *viz.*  $13 + 11 + 9 + 7 + 5 + 3 + 1 = 49$ . Now let the  $\text{Tb}^{3+}$  ion in addition to the SOC feel the crystal electric field imposed by the  $S_4$  symmetry inside the  $\text{LiTbF}_4$  crystal. In this case, the  ${}^7F_6$  multiplet splits into three nondegenerate (3nd)  $\Gamma_1$ , four nondegenerate (4nd)  $\Gamma_2$ , and three doubly degenerate (3dd)  $\Gamma_{3,4}$  irreducible representations; *viz.*  ${}^7F_6$ -multiplet  $\xrightarrow[\text{CEF}]{\text{splits}}$   $3\Gamma_1(nd) + 4\Gamma_2(nd) + 3\Gamma_{3,4}(dd)$ -irreducible representations.

The sum of the degeneracies of the irreducible representations is 13; *viz.*  $3 \times 1 + 4 \times 1 + 3 \times 2 = 13$ . Therefore, from the above discussion on  $\text{Tb}^{3+}$  ion under both of the SO and CEF interactions, the splittings of all the multiplets and their corresponding numbers of degenerate and nondegenerate irreducible representations ( $N_{\Gamma}$ ) can be compactly read as:

$$\begin{aligned}
& {}^7F \text{ multiplet} \xrightarrow[\text{CEF}]{\text{splits}} 3\Gamma_1(nd) + 4\Gamma_2(nd) + 3\Gamma_{3,4}(dd), \\
& N_{\Gamma}^{7F_6} = 3 \times 1 + 4 \times 1 + 3 \times 2 = 13, \\
& {}^7F \text{ multiplet} \xrightarrow[\text{CEF}]{\text{splits}} 3\Gamma_1(nd) + 2\Gamma_2(nd) + 3\Gamma_{3,4}(dd), \\
& N_{\Gamma}^{7F_5} = 3 \times 1 + 2 \times 1 + 3 \times 2 = 11, \\
& {}^7F \text{ multiplet} \xrightarrow[\text{CEF}]{\text{splits}} 3\Gamma_1(nd) + 2\Gamma_2(nd) + 2\Gamma_{3,4}(dd), \\
& N_{\Gamma}^{7F_4} = 3 \times 1 + 2 \times 1 + 2 \times 2 = 9, \\
& {}^7F \text{ multiplet} \xrightarrow[\text{CEF}]{\text{splits}} \Gamma_1(nd) + 2\Gamma_2(nd) + 2\Gamma_{3,4}(dd), \\
& N_{\Gamma}^{7F_3} = 1 \times 1 + 2 \times 1 + 2 \times 2 = 7, \\
& {}^7F \text{ multiplet} \xrightarrow[\text{CEF}]{\text{splits}} \Gamma_1(nd) + 2\Gamma_2(nd) + \Gamma_{3,4}(dd), \\
& N_{\Gamma}^{7F_2} = 1 \times 1 + 2 \times 1 + 1 \times 2 = 5, \\
& {}^7F \text{ multiplet} \xrightarrow[\text{CEF}]{\text{splits}} \Gamma_1(nd) + \Gamma_{3,4}(dd), \\
& N_{\Gamma}^{7F_1} = 1 \times 1 + 1 \times 2 = 3, \\
& {}^7F \text{ multiplet} \xrightarrow[\text{CEF}]{\text{splits}} \Gamma_1(nd), \\
& N_{\Gamma}^{7F_0} = 1 \times 1 = 1, \\
& N_{\Gamma}^{\text{Total}} = N_{\Gamma}^{7F_6} + N_{\Gamma}^{7F_5} + N_{\Gamma}^{7F_4} + N_{\Gamma}^{7F_3} + N_{\Gamma}^{7F_2} + N_{\Gamma}^{7F_1} + N_{\Gamma}^{7F_0}, \\
& N_{\Gamma}^{\text{Total}} = 13 + 11 + 9 + 7 + 5 + 3 + 1 = 49.
\end{aligned} \tag{13}$$

From the above expression, it can be noticed that  $N_{\Gamma}^{\text{Total}}$  in the presence of both the SO and CEF interactions is obtained to be consistently identical to the sum of the degeneracies of the multiplets in the presence of the SOC only and whence equal to the degeneracy of the free ion in the absence of the SOC. This confirms that the splittings of the multiplets are correctly performed.

The above splittings deduced from the results presented in Fig. 7(a) and the information given in Table V are in agreement with the expected splittings of the non-Kramers systems having integer  $J$ . For the non-Kramers systems, a level can split into nondegenerate states if  $M_J$  is even and doubly degenerate states if  $M_J$  is odd. As can be seen from Fig. 7(a),  ${}^7F_0$  is singlet with  $M_J = 0$  which is even. The results also show that the  ${}^7F_1$  multiplet splits into a singlet with  $M_J = 0$  which is an even number and a doublet with  $M_J = \pm 1$  which are odd numbers. Similar consistencies can be seen for the other multiplets in which their splittings under SOC+SCF interactions are discussed above and shown in Fig. 7(a). More importantly, our theoretical results are in agreement with the experimental data. This shows that the splittings can be

reproduced successfully not only for the Kramers systems but also for the non-Kramers systems by the CFP scheme. Moreover, these consistencies with the experimental data without applying LDA+ $U$  for strongly correlated systems show that the correlations among  $4f$  electrons can also be well reproduced. Gaining insights from the above discussions presented for the  $\text{Yb}^{3+}$  and  $\text{Dy}^{3+}$  ions in the Kramers  $\text{LiYbF}_4$  and  $\text{LiDyF}_4$  crystals, respectively, as well as for the  $\text{Tb}^{3+}$  ion in the non-Kramers  $\text{LiTbF}_4$  crystal, the following points can be promptly concluded from Figs. 6(b) and 6(b) and 6(c) for the remaining compounds.

### 7. $\text{LiHoF}_4$

For this non-Kramers case with integer  $J$ , Fig. 7(b) shows that the ground  ${}^5I_8$  multiplet splits into four doublet (1st, 6th, 9th, and 12th states) and nine singlet states in agreement with the prediction of group theory and Hund's rules as well as empirical data [47], see the nine empty and four solid stars in this figure. For this multiplet  $J$  is eight leading to 17  $M_J$  numbers with nine odd  $M_J$  and  $8 = 2 \times 4$  even  $M_J$  numbers. The first excited  ${}^5I_7$  multiplet splits into four doublets and seven singlets, see seven empty and four solid stars. The second excited  ${}^5I_6$  multiplet splits into four doublet and five singlet states. The third excited  ${}^5I_5$  multiplet splits into three doublet and five singlet states. The fourth excited  ${}^5I_4$  multiplet splits into two doublet and five singlet states, as shown by two solid and five empty stars. The splittings calculated by  $\Delta = -0.5$  Ry are in agreement with the Hund's rules and empirical data reported in Refs. [44,49,61].

### 8. $\text{LiTmF}_4$

For the case of non-Kramers crystal  $\text{LiTmF}_4$  with integer  $J$ , Fig. 7(c) shows that the ground state  ${}^3H_6$  multiplet splits into three doublet and seven singlet states in agreement with the empirical data reported in Ref. [47]. The ground state is not degenerate. The first excited state is  ${}^3H_4$  in contrast to the Hund's rules but in agreement with the experimental results reported in Ref. [91]. Thus, in addition to the  $\text{Dy}^{3+}$  ion, the  $\text{Tm}^{3+}$  ion can also be considered as an extraordinary case that is successfully predicted by the CFP scheme. The next  ${}^3H_4$  multiplet splits into two doublet and five singlet states. The  ${}^3H_5$  multiplet splits into four doublet and singlet states. The calculated results using  $\Delta = -0.5$  Ry are in agreement with the empirical results reported in Refs. [47,91]. For the  ${}^3H_4$  multiplet,  $J$  is 4, as indicated in Table V, and thereby  $M_J$  varies from  $-4$  to  $4$  by step 1 resulting in 9  $M_J$ ; *viz.*  $2J + 1 = 2 \times 4 + 1 = 9$ . Therefore, in the interval  $[-4, 4]$ , there are five even numbers  $M_J$ , *i.e.*,  $-4, -2, 0, 2, 4$ , and four odd numbers  $M_J$ , *i.e.*,  $-3, -1, 1, 3$ . Interestingly, our *ab initio* results clearly confirm that there are four doublets and five singlets by showing up two solid stars and five empty stars in Fig. 7(c). The two solid stars refer to the two doublets leading to four states for the four even  $M_J$ , and the five empty stars indicate five singlets for the five odd  $M_J$ . Such consistencies between the prediction of group theory and our first-principle results can be seen in the other multiplets.



### 9. $\text{LiErF}_4$

For the case of Kramers compound  $\text{LiErF}_4$  with half-integer  $J$ , Fig. 7(b) shows that all the states are doubly degenerate due to the Kramers degeneracy theorem. The ground  $^4I_{15/2}$  multiplet splits into eight double states in agreement with empirical results reported in Ref. [47]. The next  $^4I_{13/2}$  and  $^4I_{11/2}$  as well as  $^4I_{9/2}$  multiplets split into seven and six as well as five double states, respectively, in agreement with the empirical results reported in Refs. [44,62].

### 10. Summary

The following points can be concluded from the splittings presented in Figs. 6 and 7: We notice that the multiplets and their splittings are in complete accord with the prediction of group theory and Hund's rules for all the +3 rare-earth ions with the exception of  $\text{Dy}^{3+}$  ion in the Kramers  $\text{LiDyF}_4$  crystal and  $\text{Tm}^{3+}$  in the non-Kramers  $\text{LiTmF}_4$  crystal (compare Figs. 6 and 7 with Table V). Interestingly, our theoretical predictions for both of these exceptional cases which violate the Hund's rules are in complete accord with the experimental data. The calculated energy levels of the multiplets show that if  $J$  is an integer number, the multiplets of the non-Kramers systems contain two nondegenerate  $\Gamma_1$  and  $\Gamma_2$  states for even  $M_J$  as well as a doubly degenerate  $\Gamma_{3,4}$  for odd  $M_J$ , see Figs. 7(a) to 7(c) as well as  $\text{Tb}^{3+}$ ,  $\text{Ho}^{3+}$ , and  $\text{Tm}^{3+}$  ions in Table V. However, if  $J$  is a half-integer number, all the levels of the Kramers systems are doubly degenerate and their corresponding irreducible representations are  $\Gamma_{5,6}$  and  $\Gamma_{7,8}$ , see Figs. 6(a) to 6(c) as well as  $\text{Dy}^{3+}$ ,  $\text{Er}^{3+}$ , and  $\text{Yb}^{3+}$  ions in Table V. These pieces of evidence qualitatively show that the calculated splittings are consistent with the character table of the double group of the  $S_4$  symmetry and the Kramers' theorem. Furthermore, the calculated splittings are compared with the experimental data given in Figs. 7 and 6. The comparison shows that the splittings of the multiplets are in agreement with the experimental data.

## V. CONCLUSION

In this work, with the hope of introducing a new powerful *ab initio* technique for measuring small and localized magnetic field which, in turn, can play a key role in various fields in particular bio- and nanotechnology, we have calculated the crystal field parameters (CFPs) in  $\text{LiRF}_4$  ( $R = \text{Tb}, \text{Dy}, \text{Ho}, \text{Er}, \text{Tm}, \text{and Yb}$ ) using a combination of the density functional theory (DFT), CFP scheme, open-core treatment, and Wannier functions. On one side, we have noticed that these compounds due to their  $4f$  electrons may behave as strongly correlated systems. On the other side, however, we have found that the conventional band correlated schemes like  $\text{LDA}+U$  may not be applicable for this purpose due to the fixed number of electrons in the crystal field optical transitions. To this end, we have used the CFP scheme recently proposed by Pavel Novák and coworkers. To overcome the nonphysical self-interaction problem, the  $4f$  electrons are treated by the open-core scheme. We have then extracted the Wannier functions from the Bloch's eigenstates calculated by the DFT to derive the CFPs.

The behaviors of the real and imaginary parts of the CFPs are studied through the series of compounds. Employing the calculated CFPs, we find the splittings of the energy levels of the +3 rare-earth ions in the compounds by constructing an effective Hamiltonian for each case. Our calculated splittings of the multiplets of the +3 rare-earth ions using the CFP scheme are compared with the predictions of group theory and Hund's rules. The comparison shows that they are consistent with each other except for the  $\text{Dy}^{3+}$  and  $\text{Tm}^{3+}$  ions. The configurations of the multiplets of the latter ions show some deviation from the theoretical predictions of group theory and Hund's rules. It is interestingly explored that these deviations are in agreement with the available experimental data. This shows that the predictions made by the CFP scheme can reliably reproduce experimental measurements. To better improve the results, we optimize the adjustable single  $\Delta$  parameter of the CFP scheme to control the degrees of hybridizations between  $4f$  states of the rare-earth ions and the  $2p$  and  $2s$  states of the fluorine ligands. We find that hybridizations are important and should be considered.

It can be predictable that constructing an effective Hamiltonian including crystal field parameters in the presence of an external magnetic field by advanced *ab initio* techniques can provide a powerful approach for this purpose. The symmetry of the  $\text{LiRF}_4$  series of compounds considered here is  $S_4$ . To simplify the effective Hamiltonian of some cases with  $S_4$  symmetry, this symmetry can be approximated by  $D_{2d}$  symmetry. In this work, by evaluating matrix elements including in the crystal field Stevens Hamiltonian, however, we have shown that this approximation may be case dependent and it is better to use the rightful  $S_4$  symmetry than the auxiliary  $D_{2d}$  symmetry for the compounds in question.

In essence, we have obtained the whole set of seven crystal field parameters, a *new* agreement with the experimental and empirical data, and we have also provided a comprehensive comparison to the results in the literature. This may be potentially fruitful for further investigations in the active fields of the rare-earth compounds. The recent new theoretical-computational method is successfully implemented for the set of fluorides each of which is defined by hosting a different species of rare-earth ions. Such a CFP method is interesting and it challenges the very well known  $\text{LDA}+U$  in estimating the crystal-field (CF) parameters, as the experimental data are reproduced by the CFP scheme for these rare-earth-based compounds without  $\text{LDA}+U$ .

## ACKNOWLEDGMENTS

We are deeply grateful to Pavel Novák for spending his valuable time patiently to physically and computationally discuss various parts of the CFP scheme. We are also thankful to Farhad Jalali-Asadabadi for his nice graphical assistance. This work is partially supported by the University of Isfahan (UI).

## APPENDIX A: CRYSTAL STRUCTURE

$\text{LiRF}_4$  compounds crystallize in the body-centered tetragonal Scheelite  $\text{CaWO}_4$  structure with space group  $C_{4h}^6 (I4_1/a)$  [47,60]. The primitive unit cell of  $\text{LiRF}_4$ , as shown in

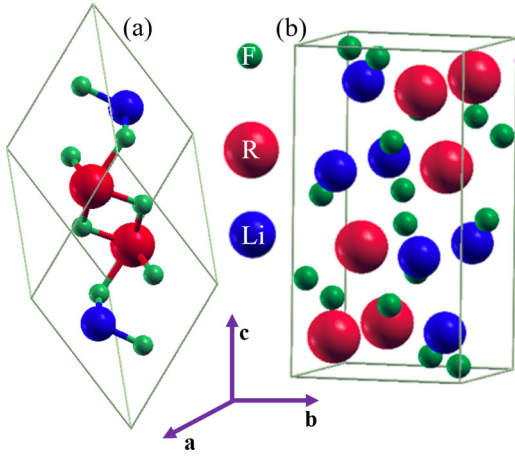


FIG. 8. (a) Primitive and (b) conventional unit cells of  $\text{LiRF}_4$  crystal.

Fig. 8(a), contains three nonequivalent, namely Li, R, and F, ions. These are arranged along two equivalent Li sites, two equivalent R sites, and eight equivalent F sites. The conventional unit cell of the  $\text{LiRF}_4$  is shown in Fig. 8(b). The site symmetry is  $S_4$  ( $\bar{4}$ ) for the Li and R ions [105] whereas the F ions do not occupy a specific site symmetry and thence the F ions have not an inversion center [60]. These compounds can be diluted by the other rare-earth ions than the R ion already existed in  $\text{LiRF}_4$  or by some nonmagnetic ions such as Y and Lu. The lattice parameters are calculated using the Perdew-Burke-Ernzerhof generalized gradient approximation (PBE-GGA) [73] excluding and including spin polarization. The PBE-GGA is a semilocal functional which has been extensively used for a variety of cases successfully. It is worth to emphasize, however, that the accuracy of the DFT plus PBE-GGA calculations depends on the localization degrees of the  $4f$  electrons in the rare-earth-based compounds [82]. To increase the accuracy of the DFT cancellations, the band correlated methods such as LDA+ $U$  [27,75–77] is usually used for the study of strongly correlated systems [34–36,81,82]. However, the LDA+ $U$  approach cannot be applied for the CFPs calculations of the rare-earth-based systems [4]. Therefore, we do not use this approach in this work. Fortunately, lattice parameters, as reported here in this section, are less sensitive to the correlation effects compared to the other properties such as magnetic properties and electric field gradients (EFGs) [34–36,81,82]. For the CFPs calculations, the open-core treatment is used to treat satisfactorily with the  $4f$  electrons of the compounds, as discussed in detail in Appendix C. The results together with the experimental data are tabulated in Table VI. The results show that the lattice parameters are also not very sensitive to the spin polarization, in agreement with our previous work on the other rare-earth-based compounds [82].

#### APPENDIX B: CONVERTING BETWEEN WYBOURNE AND STEVENS NOTATIONS

The CFPs are traditionally presented in two frequently used notations, i.e., Wybourne and Stevens notations. Our results are calculated in the Wybourne notation, whereas some of the

TABLE VI. Calculated lattice parameters in Å using PBE-GGA functional excluding and including spin polarization (SP) together with the experimental data.

Compound	a	c	SP	Expt.
$\text{LiTbF}_4$	5.246	11.007	No	
	5.260	11.029	Yes	
	5.200	10.900		[101]
$\text{LiDyF}_4$	5.227	10.926	No	
	5.232	10.921	Yes	
	5.185	10.830		[102]
$\text{LiHoF}_4$	5.237	10.884	No	
	5.237	10.901	Yes	
	5.200	10.796		[103]
$\text{LiErF}_4$	5.211	10.842	No	
	5.202	10.843	Yes	
	5.168	10.709		[103]
$\text{LiTmF}_4$	5.080	10.581	No	
	5.145	10.640		[60]
	5.133	11.026	No	
$\text{LiYbF}_4$	5.189	10.728	Yes	
	5.118	10.567		[104]

experimental and/or empirical results are given in Stevens notation. There may be several ambiguities in converting between these two notations which can make questionable the results. Therefore, here, the theoretical background presented in Sec. II is used to clarify in a transparent manner how our results are converted from the framework of Wybourne to that of Stevens by keeping in mind Eqs. (6) and (10), where their coefficients are real and therefore comparable with each other. To this end, as Eqs. (6) and (10) imply, it is necessary to know the ratios  $\mathbb{B}_q^k / (\mathbb{A}_q^k \langle r^k \rangle) = \xi_q^k$  and the Stevens factors  $\Theta^k(J)$ . Therefore, for convenience and being readily accessible, the ratios  $\xi_q^k$  are represented in Table VII [5] and the Stevens factors are also given in Table VIII [1] for the rare earth ions under study in this work only. Furthermore, both the complex Wybourne operators  $\hat{\mathbb{C}}_q^k$  and the complex Stevens equivalent operators  $\hat{\Theta}_q^k(J_x, J_y, J_z, J)$  should be known for every given  $q$  and  $k$ . The former operators,  $\hat{\mathbb{C}}_q^k$ , have already been given by Eqs. (3) and (5). Those of the latter operators  $\hat{\Theta}_q^k(J_x, J_y, J_z, J)$  used for our cases are selected and also tabulated in Table IX [1,6], for being readily available. Now everything is ready to convert Wybourne CFPs to Stevens CFPs by:

$$\mathbb{B}_{q,\text{Stev.}}^k(J) = \mathbb{B}_{q,\text{Wyb.}}^k \times \Theta^k(J) / \xi_q^k, \quad (\text{B1})$$

TABLE VII. The ratios  $\mathbb{B}_q^k / (\mathbb{A}_q^k \langle r^k \rangle) := \xi_q^k$  of the real CFPs parameterized by Wybourne in Eq. (6),  $\mathbb{B}_q^k$ , and Stevens in Eq. (10),  $\mathbb{A}_q^k \langle r^k \rangle$  [5].

k	q	$\xi_q^k = \mathbb{B}_q^k / (\mathbb{A}_q^k \langle r^k \rangle)$
2	0	2 = 2.00
4	0	8 = 8.00
4	4	$4\sqrt{70}/35 = 0.956$
6	0	16 = 16.00
6	4	$8\sqrt{14}/21 = 1.425$

TABLE VIII. The Stevens factors  $\Theta^k(J)$  of the rare earth ions under question for  $k = 2$ , i.e.,  $\alpha_j = \Theta^2(J)$ , and  $k = 4$ , i.e.,  $\beta_j = \Theta^4(J)$ , as well as  $k = 6$ , i.e.,  $\gamma_j = \Theta^6(J)$  together with the total angular quantum number  $J$  determined for each ion [1].

$R^{3+}$	$J$	$\Theta^2(J)$	$\Theta^4(J)$	$\Theta^6(J)$
Tb <sup>3+</sup>	6	$\frac{-1}{3^2 \times 11}$	$\frac{2}{3^3 \times 5 \times 11^2}$	$\frac{-1}{3^4 \times 7 \times 11^2 \times 13}$
Dy <sup>3+</sup>	15/2	$\frac{-2}{3^2 \times 5 \times 7}$	$\frac{-2^3}{3^3 \times 5 \times 7 \times 11 \times 13}$	$\frac{2^2}{3^3 \times 7 \times 11^2 \times 13^2}$
Ho <sup>3+</sup>	8	$\frac{-1}{2 \times 3^2 \times 5^2}$	$\frac{-1}{2 \times 3 \times 5 \times 7 \times 11 \times 13}$	$\frac{-5}{3^3 \times 7 \times 11^2 \times 13^2}$
Er <sup>3+</sup>	15/2	$\frac{2^2}{3^2 \times 5^2 \times 7}$	$\frac{2}{3^2 \times 5 \times 7 \times 11 \times 13}$	$\frac{2^3}{3^3 \times 7 \times 11^2 \times 13^2}$
Tm <sup>3+</sup>	6	$\frac{1}{3^2 \times 11}$	$\frac{2^3}{3^4 \times 5 \times 11^2}$	$\frac{-5}{3^4 \times 7 \times 11^2 \times 13}$
Yb <sup>3+</sup>	7/2	$\frac{2}{3^2 \times 7}$	$\frac{-2}{3 \times 5 \times 7 \times 11}$	$\frac{2^2}{3^3 \times 7 \times 11 \times 13}$

where  $\mathbb{B}_{q, \text{Wyb.}}^k$  are the Wybourne CFPs as defined in Eq. (6),  $\mathbb{B}_{q, \text{Stev.}}^k(J)$  are the Stevens CFPs as defined in Eq. (11),  $\Theta^k(J)$  are the Stevens factors as tabulated in Table VIII, and  $\xi_q^k$  are the ratios  $\mathbb{B}_q^k / (\mathbb{A}_q^k(r^k))$  as tabulated in Table VII for the given  $q$ ,  $k$ , and  $J$ .

It would be worthwhile to indicate the following three technical points: First, the unit of our calculated Wybourne CFPs is  $\text{cm}^{-1}$  by default, while it is  $\text{meV}$  in some references. In such cases, if any, for convenience our calculated Wybourne CFPs are multiplied by  $\frac{0.123984 \text{ meV}}{1 \text{ cm}^{-1}}$  for converting from  $\text{cm}^{-1}$  to  $\text{meV}$ . Second, in some references [47,56,97], the crystal field Hamiltonian expressed in Eq. (11) for the  $S_4$  symmetry of the systems in question is represented as follows:

$$\hat{H}_{\text{CF}} = \sum_{k=2,4,6} \mathbb{B}_0^k \hat{O}_0^k + \sum_{k=4,6} \mathbb{B}_4^k(c) \hat{O}_4^k(c) + \sum_{k=4,6} \mathbb{B}_4^k(s) \hat{O}_4^k(s), \quad (\text{B2})$$

where the argument  $c$  ( $s$ ) stands for positive (negative)  $q$  so that  $\hat{O}_4^k(c)$  ( $\hat{O}_4^k(s)$ ) operators used in the above equation are identical to  $\hat{O}_4^k$  ( $\hat{O}_{-4}^k$ ) operators used in Eq. (11) for  $k = 4$  and  $6$  [6]. By considering the latter relations, like Eq. (11) as discussed above, Eq. (B2) can be straightforwardly used for converting between Wybourne and Stevens CFPs, as well.

TABLE IX. The Stevens equivalent operators  $\hat{O}_q^k(J_x, J_y, J_z, J)$ , where  $J_{\pm} \equiv J_x \pm iJ_y$ , and  $X \equiv J(J+1)$  [1,6].

$k$	$q$	$\hat{O}_q^k(J_x, J_y, J_z, J)$
2	0	$3J_z^2 - X$
4	0	$35J_z^4 - (30X - 25)J_z^2 + 3X^2 - 6X$
4	-4	$\frac{1}{2i}(J_+^4 - J_-^4)$
4	4	$\frac{1}{2}(J_+^4 + J_-^4)$
6	0	$231J_z^6 - (315X - 735)J_z^4 + (105X^2 - 525X + 294)J_z^2 - 5X^3 + 40X^2 - 60X$
6	-4	$\frac{1}{4i}[(11J_z^2 - X - 38)(J_+^4 - J_-^4) + (J_+^4 - J_-^4)(11J_z^2 - X - 38)]$
6	4	$\frac{1}{4}[(11J_z^2 - X - 38)(J_+^4 + J_-^4) + (J_+^4 + J_-^4)(11J_z^2 - X - 38)]$

Third, the experimental data are not usually sufficient to obtain all the seven CFPs of the  $S_4$  point symmetry. Thus, in such a case, it can be tried to reduce the number of CFPs. To this end, there are two custom ways:

(i) The first way [5,47,85] is to apply the following unitary transformation on the Stevens Hamiltonian  $\hat{H}_{\text{CF}}$  expressed in Eq. (11) so that one of the CFPs can be neglected:

$$\hat{H}'_{\text{CF}} := \hat{U}^\dagger \hat{H}_{\text{CF}} \hat{U} = \sum_{k=2,4,6} \mathbb{B}_0^k \hat{U}^\dagger \hat{O}_0^k \hat{U} + \mathbb{B}_{-4}^4 \hat{U}^\dagger \hat{O}_{-4}^4 \hat{U} + \mathbb{B}_4^4 \hat{U}^\dagger \hat{O}_4^4 \hat{U} + \mathbb{B}_{-4}^6 \hat{U}^\dagger \hat{O}_{-4}^6 \hat{U} + \mathbb{B}_4^6 \hat{U}^\dagger \hat{O}_4^6 \hat{U}, \quad (\text{B3})$$

where  $\hat{H}'_{\text{CF}}$  is the transformed Stevens Hamiltonian and  $\hat{U} = \exp(-i\varphi J_z)$  is the unitary rotation operator about the Cartesian  $z$  axis by a suitable angle  $\varphi$ . By this unitary transformation, the Stevens  $\hat{O}_0^k$  operators remain unchanged, because the  $\hat{O}_0^k$  operators commute with  $\hat{U}$ , viz.  $[\hat{O}_0^k, \hat{U}] = 0$  or equivalently  $\hat{U}^\dagger \hat{O}_0^k \hat{U} = \hat{O}_0^k$ . The other remaining operators, i.e.,  $\hat{O}_{-4}^4$  and  $\hat{O}_4^4$  as well as  $\hat{O}_{-4}^6$  and  $\hat{O}_4^6$ , are changed according to the transformation relations derived by Czeslaw Rudowicz [85], which are tabulated in Table X for  $k = 4, 6$  and  $q = \pm 4$ . Hence, using  $\hat{U}^\dagger \hat{O}_0^k \hat{U} = \hat{O}_0^k$  and the transformation relations given in Table X, Eq. (B3) can be read as:

$$\begin{aligned} \hat{H}'_{\text{CF}} &= \sum_{k=2,4,6} \mathbb{B}_0^k \hat{O}_0^k \\ &+ \mathbb{B}_{-4}^4 [ + \cos(4\varphi) \hat{O}_{-4}^4 + \sin(4\varphi) \hat{O}_4^4 ] \\ &+ \mathbb{B}_4^4 [ - \sin(4\varphi) \hat{O}_{-4}^4 + \cos(4\varphi) \hat{O}_4^4 ] \\ &+ \mathbb{B}_{-4}^6 [ + \cos(4\varphi) \hat{O}_{-4}^6 + \sin(4\varphi) \hat{O}_4^6 ] \\ &+ \mathbb{B}_4^6 [ - \sin(4\varphi) \hat{O}_{-4}^6 + \cos(4\varphi) \hat{O}_4^6 ] \quad (\text{B4}) \\ &:= \sum_{k=2,4,6} \mathbb{B}_0^k \hat{O}_0^k \\ &+ \mathbb{B}_{-4}^4 \hat{O}_{-4}^4 + \mathbb{B}_4^4 \hat{O}_4^4 + \mathbb{B}_{-4}^6 \hat{O}_{-4}^6 + \mathbb{B}_4^6 \hat{O}_4^6, \quad (\text{B5}) \end{aligned}$$

where  $\hat{O}_q^k$  are defined to be  $\hat{U}^\dagger \hat{O}_q^k \hat{U}$  as tabulated in Table X. Therefore, Eqs. (B4) and (B5) can be rearranged as:

$$\begin{aligned} \hat{U}^\dagger \hat{H}_{\text{CF}} \hat{U} &= \sum_{k=2,4,6} \mathbb{B}_0^k \hat{O}_0^k \\ &+ [\cos(4\varphi) \mathbb{B}_{-4}^4 - \sin(4\varphi) \mathbb{B}_4^4] \hat{O}_{-4}^4 \\ &+ [\sin(4\varphi) \mathbb{B}_{-4}^4 + \cos(4\varphi) \mathbb{B}_4^4] \hat{O}_4^4 \\ &+ [\cos(4\varphi) \mathbb{B}_{-4}^6 - \sin(4\varphi) \mathbb{B}_4^6] \hat{O}_{-4}^6 \\ &+ [\sin(4\varphi) \mathbb{B}_{-4}^6 + \cos(4\varphi) \mathbb{B}_4^6] \hat{O}_4^6 \quad (\text{B6}) \\ &:= \sum_{k=2,4,6} \mathbb{B}_0^k \hat{O}_0^k \\ &+ \mathbb{B}_{-4}^4 \hat{O}_{-4}^4 + \mathbb{B}_4^4 \hat{O}_4^4 + \mathbb{B}_{-4}^6 \hat{O}_{-4}^6 + \mathbb{B}_4^6 \hat{O}_4^6, \quad (\text{B7}) \end{aligned}$$

where  $\mathbb{B}_q^k$  can be straightforwardly defined by comparing Eqs. (B6) and (B7), see Table X. From Eq. (B5), the Stevens  $\hat{O}_q^k$  operators can be interpreted as tensors which are rotated to  $\hat{O}_q^k$  about the  $z$  axis by an angle  $\varphi$  while the  $\mathbb{B}_q^k$  CFPs are kept fixed. Interestingly, by considering Eq. (B7), however,

TABLE X. The Rudowicz transformation relations [85] of the Stevens operators. The rotated CFP tensors as defined by comparing Eqs. (B6) and (B7).

$k$	$q$	$\hat{U}^\dagger \hat{O}_q^k \hat{U} := \hat{O}_q^k$	$\tilde{\mathbb{B}}_q^k$
4	-4	$+\cos(4\varphi)\hat{O}_{-4}^4 + \sin(4\varphi)\hat{O}_4^4$	$\cos(4\varphi)\tilde{\mathbb{B}}_{-4}^4 - \sin(4\varphi)\tilde{\mathbb{B}}_4^4$
4	4	$-\sin(4\varphi)\hat{O}_{-4}^4 + \cos(4\varphi)\hat{O}_4^4$	$\sin(4\varphi)\tilde{\mathbb{B}}_{-4}^4 + \cos(4\varphi)\tilde{\mathbb{B}}_4^4$
6	-4	$+\cos(4\varphi)\hat{O}_{-4}^6 + \sin(4\varphi)\hat{O}_4^6$	$\cos(4\varphi)\tilde{\mathbb{B}}_{-4}^6 - \sin(4\varphi)\tilde{\mathbb{B}}_4^6$
6	4	$-\sin(4\varphi)\hat{O}_{-4}^6 + \cos(4\varphi)\hat{O}_4^6$	$\sin(4\varphi)\tilde{\mathbb{B}}_{-4}^6 + \cos(4\varphi)\tilde{\mathbb{B}}_4^6$

the crystal field parameters  $\tilde{\mathbb{B}}_q^k$  can be conversely interpreted as tensors which are rotated to  $\tilde{\mathbb{B}}_q^k$  about the  $z$  axis in the opposite direction by an angle  $-\varphi$  while this time the Stevens  $\hat{O}_q^k$  operators are kept fixed. These interpretations originate from the existed symmetry between the appearance of  $\tilde{\mathbb{B}}_q^k$  and  $\hat{O}_q^k$  as their product  $\tilde{\mathbb{B}}_q^k \hat{O}_q^k$  in the Hamiltonian  $\hat{H}_{\text{CF}}$ . For sure, both of the above interpretations are identical. However, the second one can be more preferable, since in this way the number of CFPs can be reduced by choosing a suitable  $\varphi$  angle. To this end,  $\tilde{\mathbb{B}}_{-4}^4$  in Eq. (B7) can be forced to be zero:

$$\cos(4\varphi)\tilde{\mathbb{B}}_{-4}^4 - \sin(4\varphi)\tilde{\mathbb{B}}_4^4 = 0, \quad (\text{B8})$$

which yields the  $\varphi$  angle as:

$$\varphi = \frac{1}{4} \tan^{-1} \left( \frac{\tilde{\mathbb{B}}_{-4}^4}{\tilde{\mathbb{B}}_4^4} \right). \quad (\text{B9})$$

This equation implies that  $\varphi$  is case dependent and should be determined for every compound individually by Eq. (B9). After setting  $\varphi$  by this equation, only six CFPs (among the seven CFPs of the  $S_4$  point symmetry) will remain to be determined for each compound. In this work, we do not have any limitations and can determine all seven Stevens  $\tilde{\mathbb{B}}_q^k$  CFPs by converting our calculated Wybourne  $\mathbb{B}_q^k$  real CFPs using Eq. (B1), as discussed earlier. To compare our converted Stevens CFPs with the experimental references where only six nonzero CFPs are reported, however, we should also inevitably utilize Eq. (B9) to set  $\tilde{\mathbb{B}}_{-4}^4 = 0$  and determine the  $\varphi$  angle. Then, using the determined  $\varphi$ , we transform our converted Stevens CFPs from  $\mathbb{B}_4^4, \mathbb{B}_4^6, \mathbb{B}_{-4}^6$  to  $\tilde{\mathbb{B}}_4^4, \tilde{\mathbb{B}}_4^6, \tilde{\mathbb{B}}_{-4}^6$  using the relations given in Table X.

(ii) The second way to reduce the number of CFPs is to consider the higher point symmetry  $D_{2d}$  for the +3 rare-earth rather than the lower point symmetry  $S_4$  [44,49,61–64]. This way also works, because the  $D_{2d}$  is not only close to  $S_4$  symmetry but also requires only five CFPs to be determined. For  $D_{2d}$  symmetry, the crystal field Hamiltonian reads:

$$\hat{H}_{\text{CF}} = \sum_{k=2,4,6} \mathbb{B}_0^k \hat{O}_0^k + \sum_{k=4,6} \mathbb{B}_4^k \hat{O}_4^k, \quad (\text{B10})$$

where the two terms with  $q < 0$  are not presented any more; *viz.* in the language of Eq. (B2)  $\mathbb{B}_4^k(s) = 0$  for both  $k = 4$  and 6. Therefore, it appears that this might be a reasonable approximation, if by considering the  $S_4$  symmetry the  $\mathbb{B}_4^k(s)$  CFPs are much less than those of the other terms. In Sec. IV C, however, the validity of this approximation is examined for the cases under study by considering their actual  $S_4$  symmetry. To this end, for sure, the matrix elements of the Stevens

Hamiltonian are analytically derived term by term and accordingly discussed in Sec. IV C, see Table II.

Using the information represented in this Appendix, first, the Wybourne CFPs are converted to the Stevens notation according to Eqs. (B1), (6), (11) as well as Tables VII and VIII, as discussed above and Sec. II. Second, the unit of the CFPs is converted from  $\text{cm}^{-1}$  to meV using the conversion factor aforementioned in this Appendix. The converted CFPs are tabulated in Table XI both in the absence and presence of the hybridization for all the compounds. The hybridization is applied by the optimized  $\Delta = -0.5 \text{ Ry}$  parameter. Third, the Stevens CFPs are transformed using the Czeslaw Rudowicz transformation relations [85], as discussed in this Appendix and represented in Table X. In order to apply the Rudowicz transformation, the rotational angles  $\varphi$  are obtained by Eq. (B9), as discussed above in this Appendix. The angles  $\varphi$  are also tabulated in Table XI.

### APPENDIX C: COMPUTATIONAL DETAILS

The band structure calculations are performed in the framework of the density functional theory (DFT) [23,24] using the APW plus local orbital (APW+lo) method [78–80] employing the PBE-GGA functional [73] as implemented in the WIEN2K code [106,107] for all the cases under study. Spin dependencies of the CFPs were reported to be negligible for  $\text{PrO}_2$  [9] and  $\text{SmCo}_5$  [14]. Furthermore, the CFPs of the rare-earth aluminates were also recently reported in agreement with the experiments without considering spin polarization [4]. Therefore, based on the practical evidence and the CFP recipe [4,38,39,41] on the approximately negligible effects of spin polarization on the values of CFPs, non-spin-polarized CFPs calculations are performed, though the CFPs can principally depend on spin configurations. The muffin-tin radii ( $R_{\text{MT}}$ 's) in a.u. are tabulated in Table XII, as selected for Li, R, and F ions in  $\text{LiRf}_4$  compounds. For the calculations of the structural properties, a mesh of 200 special  $k$  points is considered in the irreducible wedge of the first Brillouin (1BZ) zone which corresponds to the grids of  $5 \times 5 \times 5$  in the Monkhorst-Pack scheme [108]. For the crystal field calculations, a denser  $k$  mesh including 1000 special  $k$  points is considered in the irreducible wedge of the 1BZ corresponding to the grids of  $10 \times 10 \times 10$ . The cutoff parameter of  $K_{\text{max}} = 8/R_{\text{MT}}$  ( $l_{\text{max}} = 10$ ) inside the muffin-tin spheres (interstitial region) is used for the expansions of the wave functions in terms of the lattice harmonics (plane waves). The periodic charge density and potential are Fourier expanded up to  $G_{\text{max}} = 13 \text{ Bohr}^{-1}$ . The DOSs are regularly calculated for  $4f$  electrons using the PBE-GGA, as shown in Figs. 1(a)–1(d) for  $\text{LiErF}_4$ . By

TABLE XI. Converted Wybourne crystal field parameters (CFPs) to Stevens CFPs, as expressed by Eq. (11), in meV for the +3 rare-earth in LiRF<sub>4</sub> compounds without and with the optimized hybridization  $\Delta$  parameters. The case dependent angle  $\varphi$  is calculated by Eq. (B9) for each case. The conversions from Wybourne to Stevens notation are performed by considering Eq. (B1) and the ratios  $\xi_q^k$  given in Table VII as well as the Stevens factors  $\Theta^k(J)$  represented in Table VIII.

LiRF <sub>4</sub>	$\Delta$	$10^3 \times \tilde{B}_0^2$	$10^3 \times \tilde{B}_0^4$	$10^3 \times \tilde{B}_4^4$	$10^3 \times \tilde{B}_{-4}^4$	$10^6 \times \tilde{B}_0^6$	$10^6 \times \tilde{B}_4^6$	$10^6 \times \tilde{B}_{-4}^6$	$\varphi$ (rad)
LiTbF <sub>4</sub>	0	-322	-1.68	-12.4	-11.1	-0.210	76.2	56.2	0.182
	-0.5	-304	-1.38	-10.6	-9.51	-0.165	60.1	43.7	0.183
LiDyF <sub>4</sub>	0	-163	0.817	5.91	4.84	0.588	-70.0	-48.7	0.171
	-0.5	-155	0.696	5.23	4.32	0.492	-57.7	-39.5	0.173
LiHoF <sub>4</sub>	0	-58.4	0.389	2.95	2.61	-0.538	74.6	51.7	0.181
	-0.5	-56.3	0.339	2.66	2.37	-0.421	62.7	42.9	0.182
LiErF <sub>4</sub>	0	61.8	-0.511	-3.75	-3.09	1.03	-114	-77.8	0.172
	-0.5	60.3	-0.462	-3.50	-2.91	0.853	-99.8	-67.0	0.173
LiTmF <sub>4</sub>	0	206	-0.883	-7.16	-6.56	-0.821	137	93.2	0.182
	-0.5	240	-1.67	-13.0	-12.0	-1.71	273	177	0.187
LiYbF <sub>4</sub>	0	707	15.5	128	117	35.7	-6555	-4662	0.186
	-0.5	699	14.8	126	117	28.5	-6143	-4288	0.187

regular, we mean the standard DFT calculations where no special treatment such as open core is still considered for the 4*f* electrons. The regular DOSs show that the 4*f*-Er states are present in the valence region and peaked up nearby the Fermi level, as expected from the semilocal PBE-GGA functional.

As the *first step* of the CFP scheme, in addition to the regular DOSs, the DOSs are also recalculated employing the open-core treatment by confining the 4*f* electrons into the core using the PBE-GGA, as shown in Figs. 1(e)–1(h) for LiErF<sub>4</sub>. The Kohn-Sham potential obtained in the *first step* using open core calculations, where hybridization between 4*f*-R sates and valences states are prevented by confining the 4*f* electrons into the core region, is stored to be used in the next *second step*.

In the *second step* of the CFP scheme, we aim to construct and diagonalize an effective Hamiltonian to obtain eigenvalues and Bloch eigenstates  $\psi_{nk}(\mathbf{r})$  with the band index *n* and wave vector  $\mathbf{k}$ . This Hamiltonian includes the Kohn-Sham potentials, as self-consistently obtained from and stored in the last step. It is so effectively engineered that can well describe the 4*f* states of the R ions hybridized with the 2*p* and 2*s* states of F ion. To this end, the 4*f* electrons are released from the core region. Then, a suitable orbital dependent potential is applied to all the valence states. By this potential, we push the states towards deeper energies with respect to the Fermi surface. Another task of this positive potential is to eject the other irrelevant valence states so that the 4*f* states can be

hybridized only with the relevant 2*p* and 2*s* states determined by the *first step*. At this stage, the effective Hamiltonian is more finely improved by applying the adjustable parameter  $\Delta$ , as discussed in Sec. IV D. At the end of this step, the eigenvalues and Bloch eigenfunctions are obtained for the 4*f* states and stored to be used in the next step.

In the *third step*, the 4*f*-band Bloch eigenfunctions  $\psi_{nk}(\mathbf{r})$  obtained in the *second step* are Fourier transformed over the first Brillouin zone (1BZ) to the *m*th Wannier functions  $W_{m\mathbf{R}}(\mathbf{r})$  with lattice vectors  $\mathbf{R}$  as follows:

$$W_{m\mathbf{R}}(\mathbf{r}) = \int_{1\text{BZ}} \left( \sum_n U_{nm}^{(\mathbf{k})} \psi_{nk}(\mathbf{r}) \right) e^{i\mathbf{k}\cdot\mathbf{R}} \frac{d\mathbf{k}}{(2\pi)^3 \Omega}, \quad (\text{C1})$$

using the WANNIER90 code [30–33] and WIEN2WANNIER code [109], where  $\Omega$  and  $(2\pi)^3/\Omega$  are the volumes of the unit cells in the direct (real) and reciprocal spaces, respectively, and  $U_{nm}^{(\mathbf{k})}$  are the matrix elements of the unitary operator *U* describing the rotation among the Bloch bands at each  $\mathbf{k}$  point. The latter code [109] plays an efficient role as an interface between the FP-LAPW WIEN2K code [106,107] and the WANNIER90 code [30–33] to construct the maximally localized Wannier functions (MLWFs) [32]. The  $U_{nm}^{(\mathbf{k})}$  are chosen so that the sum over the squares of the fluctuations in position operator under Wannier functions,  $F_{\mathbf{R}} \equiv \sum_{m=1}^7 \langle (\Delta\mathbf{r})_m^2 \rangle$ , is minimized as follows:

$$F_{\mathbf{R}} = \sum_{m=1}^7 [\langle r^2 \rangle_m - \langle \mathbf{r} \rangle_m^2] = \sum_{m=1}^7 [\langle W_{m\mathbf{R}} | r^2 | W_{m\mathbf{R}} \rangle - \langle W_{m\mathbf{R}} | r | W_{m\mathbf{R}} \rangle^2], \quad (\text{C2})$$

where  $\langle (\Delta\mathbf{r})_m^2 \rangle$  as the expression shown in the bracket is the quadratic spread of the *m*th Wannier functions in real space. After finding  $U_{nm}^{(\mathbf{k})}$  from Eq. (C2), the MLWFs [32] will be then straightforwardly determined using Eq. (C1).

TABLE XII. The Muffin-Tin radii ( $R_{\text{MT}}$ 's) in a.u. selected for Li, R and F ions in LiRF<sub>4</sub> compounds.

LiRF <sub>4</sub>	Li	R	F
LiTbF <sub>4</sub>	1.58	2.29	1.97
LiDyF <sub>4</sub>	1.56	2.29	1.97
LiHoF <sub>4</sub>	1.58	2.29	1.97
LiErF <sub>4</sub>	1.57	2.28	1.96
LiTmF <sub>4</sub>	1.56	2.26	1.94
LiYbF <sub>4</sub>	1.55	2.24	1.93

In the CFP scheme, the real states  $|\phi_i\rangle$  for  $i = 1$  to 7 are constructed by combining the complex states  $|lm\rangle$  as follows:

$$\begin{aligned} \langle\theta, \varphi|\phi_1\rangle &= \frac{i}{\sqrt{2}}[Y_{-3}^3(\theta, \varphi) + Y_3^3(\theta, \varphi)] \\ &= \frac{i}{\sqrt{2}}\left[\frac{1}{8}\sqrt{\frac{35}{\pi}}\frac{(x-iy)^3}{r^3} + \frac{-1}{8}\sqrt{\frac{35}{\pi}}\frac{(x+iy)^3}{r^3}\right] \\ &= \frac{i}{\sqrt{2}}\frac{1}{8}\sqrt{\frac{35}{\pi}}\frac{1}{r^3}[(x-iy)^3 - (x+iy)^3] \\ &= \frac{i}{\sqrt{2}}\frac{1}{8}\sqrt{\frac{35}{\pi}}\frac{1}{r^3}[(-2iy)(3x^2 - y^2)] \\ &= \frac{1}{\sqrt{2}}\frac{1}{4}\sqrt{\frac{35}{\pi}}\frac{1}{r^3}[y(3x^2 - y^2)] \\ &\propto y(3x^2 - y^2), \end{aligned} \quad (C3)$$

$$\begin{aligned} \langle\theta, \varphi|\phi_2\rangle &= \frac{1}{\sqrt{2}}[Y_{-3}^3(\theta, \varphi) - Y_3^3(\theta, \varphi)] \\ &= \frac{1}{\sqrt{2}}\left[\frac{1}{8}\sqrt{\frac{35}{\pi}}\frac{(x-iy)^3}{r^3} - \frac{-1}{8}\sqrt{\frac{35}{\pi}}\frac{(x+iy)^3}{r^3}\right] \\ &= \frac{1}{\sqrt{2}}\frac{1}{8}\sqrt{\frac{35}{\pi}}\frac{1}{r^3}[(x-iy)^3 + (x+iy)^3] \\ &= \frac{1}{\sqrt{2}}\frac{1}{8}\sqrt{\frac{35}{\pi}}\frac{1}{r^3}[(2x)(x^2 - 3y^2)] \\ &= \frac{1}{\sqrt{2}}\frac{1}{4}\sqrt{\frac{35}{\pi}}\frac{1}{r^3}[x(x^2 - 3y^2)] \\ &\propto x(x^2 - 3y^2), \end{aligned} \quad (C4)$$

$$\begin{aligned} \langle\theta, \varphi|\phi_3\rangle &= \frac{i}{\sqrt{2}}[Y_{-1}^3(\theta, \varphi) + Y_1^3(\theta, \varphi)] \\ &= \frac{i}{\sqrt{2}}\left[\frac{1}{8}\sqrt{\frac{21}{\pi}}\left(\frac{(x-iy)}{r^3} - \frac{(x+iy)}{r^3}\right)(5z^2 - r^2)\right] \\ &= \frac{i}{\sqrt{2}}\frac{1}{8}\sqrt{\frac{21}{\pi}}\frac{1}{r^3}[(-2iy)(5z^2 - r^2)] \\ &= \frac{1}{\sqrt{2}}\frac{1}{4}\sqrt{\frac{21}{\pi}}\frac{1}{r^3}[y(5z^2 - r^2)] \propto y(5z^2 - r^2) \\ &\propto yz^2, \end{aligned} \quad (C5)$$

$$\begin{aligned} \langle\theta, \varphi|\phi_4\rangle &= \frac{1}{\sqrt{2}}[Y_{-1}^3(\theta, \varphi) - Y_1^3(\theta, \varphi)] \\ &= \frac{1}{\sqrt{2}}\left[\frac{1}{8}\sqrt{\frac{21}{\pi}}\left(\frac{(x-iy)}{r^3} + \frac{(x+iy)}{r^3}\right)(5z^2 - r^2)\right] \\ &= \frac{1}{\sqrt{2}}\frac{1}{8}\sqrt{\frac{21}{\pi}}\frac{1}{r^3}[(2x)(5z^2 - r^2)] \\ &= \frac{1}{\sqrt{2}}\frac{1}{4}\sqrt{\frac{21}{\pi}}\frac{1}{r^3}[x(5z^2 - r^2)] \propto x(5z^2 - r^2) \\ &\propto xz^2, \end{aligned} \quad (C6)$$

$$\begin{aligned} \langle\theta, \varphi|\phi_5\rangle &= \frac{1}{\sqrt{2}}[Y_{-2}^3(\theta, \varphi) + Y_2^3(\theta, \varphi)] \\ &= \frac{1}{\sqrt{2}}\left[\frac{1}{4}\sqrt{\frac{105}{2\pi}}\frac{(x-iy)^2z}{r^3} + \frac{1}{4}\sqrt{\frac{105}{2\pi}}\frac{(x+iy)^2z}{r^3}\right] \\ &= \frac{1}{\sqrt{2}}\frac{1}{2}\sqrt{\frac{105}{2\pi}}\frac{1}{r^3}[z(x^2 - y^2)] \\ &\propto z(x^2 - y^2), \end{aligned} \quad (C7)$$

$$\begin{aligned} \langle\theta, \varphi|\phi_6\rangle &= \frac{i}{\sqrt{2}}[Y_{-2}^3(\theta, \varphi) - Y_2^3(\theta, \varphi)] \\ &= \frac{i}{\sqrt{2}}\left[\frac{1}{4}\sqrt{\frac{105}{2\pi}}\frac{(x-iy)^2z}{r^3} - \frac{1}{4}\sqrt{\frac{105}{2\pi}}\frac{(x+iy)^2z}{r^3}\right] \\ &= \frac{i}{\sqrt{2}}\frac{1}{4}\sqrt{\frac{105}{2\pi}}\frac{1}{r^3}[z(-4ixy)] \\ &= \frac{1}{\sqrt{2}}\sqrt{\frac{105}{2\pi}}\frac{1}{r^3}[z(xy)] \\ &\propto xyz, \end{aligned} \quad (C8)$$

$$\begin{aligned} \langle\theta, \varphi|\phi_7\rangle &= Y_0^3(\theta, \varphi) = \frac{1}{4}\sqrt{\frac{7}{\pi}}\frac{z(5z^2 - 3r^2)}{r^3} \\ &= \frac{1}{4}\sqrt{\frac{7}{\pi}}\frac{1}{r^3}z(5z^2 - 3r^2) \\ &\propto z^3. \end{aligned} \quad (C9)$$

The angular parts of the wave functions  $\langle\theta, \varphi|\psi_j\rangle$  are expanded using the above real tesseral spherical harmonics  $\langle\theta, \varphi|\phi_i\rangle$  as the bases of the 4f orbitals of the R ions for  $i = 1$  to 7 as:

$$\langle\theta, \varphi|\psi_j\rangle = \sum_{i=1}^7 c_{ij} \langle\theta, \varphi|\phi_i\rangle, \quad j = 1 - 7. \quad (C10)$$

- [1] J. Jensen and A. Mackintosh, *Rare Earth Magnetism: Structures and Excitations*, International Series of Monographs on Physics (Clarendon Press, Oxford, 1991).  
[2] D. Budker, *Nature (London)* **422**, 574 (2003).

- [3] A. Furrer, *Crystal Field Effects in Metals and Alloys* (Plenum Press, New York, 1977).  
[4] P. Novák, K. Knížek, and J. Kuneš, *Phys. Rev. B* **87**, 205139 (2013).

- [5] J. Mulak and Z. Gajek, *The Effective Crystal Field Potential* (Elsevier, New York, 2000).
- [6] M. Hutchings, *Point-Charge Calculations of Energy Levels of Magnetic Ions in Crystalline Electric Fields* (Academic Press, 1964), pp. 227–273.
- [7] D. J. Newman and B. Ng, *Rep. Prog. Phys.* **52**, 699 (1989).
- [8] O. Malta, *Chem. Phys. Lett.* **87**, 27 (1982).
- [9] P. Novák, *Rare Earth: New Research* (Nova Science Publishers, New York, 2013).
- [10] K. Ogasawara, S. Watanabe, H. Toyoshima, and M. G. Brik, in *Handbook on Physics and Chemistry of Rare Earths*, edited by Karl A. Gschneidner, J.-C. Bünzli, and V. K. Pecharsky, Handbook on the Physics and Chemistry of Rare Earths, Vol. 37 (Elsevier, North-Holland, 2007), Chap. 231, pp. 1–59.
- [11] M. Slota, S.-D. Jiang, E. Heintze, Y. Rechkemmer, M. Dressel, J. van Slageren, and L. Bogani, *Phys. Rev. B* **99**, 134410 (2019).
- [12] P. Novák and J. Kuriplach, *Phys. Rev. B* **50**, 20851994.
- [13] L. Steinbeck, M. Richter, U. Nitzsche, and H. Eschrig, *Phys. Rev. B* **53**, 7111 (1996).
- [14] P. Novák, *Physica Status Solidi (b)* **198**, 729 (1996).
- [15] T. Ishii, M. Brik, and K. Ogasawara, *J. Alloys Compd.* **380**, 136 (2004), proceedings of the 4th International Spring Workshop on Spectroscopy, Structure and Synthesis of Rare Earth Systems.
- [16] C. Rudowicz and J. Qin, *Phys. Rev. B* **67**, 174420 (2003).
- [17] L. Ning and G. P. Brivio, *Phys. Rev. B* **75**, 235126 (2007).
- [18] L. Hu, M. F. Reid, C.-K. Duan, S. Xia, and M. Yin, *J. Phys.: Condens. Matter* **23**, 045501 (2011).
- [19] L. Ungur and L. F. Chibotaru, *Chem. Eur. J.* **23**, 3708 (2017).
- [20] E. Mihóková, P. Novák, and V. V. Laguta, *J. Rare Earths* **33**, 1316 (2015).
- [21] G. Krizman, T. Schumann, S. Tchoumakov, B. A. Assaf, S. Stemmer, L. A. de Vaultier, and Y. Guldner, *Phys. Rev. B* **100**, 155205 (2019).
- [22] S. Poncé, D. Jena, and F. Giustino, *Phys. Rev. Lett.* **123**, 096602 (2019).
- [23] P. Hohenberg and W. Kohn, *Phys. Rev.* **136**, B864 (1964).
- [24] W. Kohn and L. J. Sham, *Phys. Rev.* **140**, A1133 (1965).
- [25] J. P. Perdew and A. Zunger, *Phys. Rev. B* **23**, 5048 (1981).
- [26] A. Svane, *Phys. Rev. B* **53**, 4275 (1996).
- [27] V. I. Anisimov, J. Zaanen, and O. K. Andersen, *Phys. Rev. B* **44**, 943 (1991).
- [28] A. D. Becke, *J. Chem. Phys.* **98**, 5648 (1993).
- [29] A. D. Becke, *J. Chem. Phys.* **98**, 1372 (1993).
- [30] A. A. Mostofi, J. R. Yates, Y.-S. Lee, I. Souza, D. Vanderbilt, and N. Marzari, *Comput. Phys. Commun.* **178**, 685 (2008).
- [31] A. A. Mostofi, J. R. Yates, G. Pizzi, Y.-S. Lee, I. Souza, D. Vanderbilt, and N. Marzari, *Comput. Phys. Commun.* **185**, 2309 (2014).
- [32] N. Marzari and D. Vanderbilt, *Phys. Rev. B* **56**, 12847 (1997).
- [33] I. Souza, N. Marzari, and D. Vanderbilt, *Phys. Rev. B* **65**, 035109 (2001).
- [34] S. J. Asadabadi, S. Cottenier, H. Akbarzadeh, R. Saki, and M. Rots, *Phys. Rev. B* **66**, 195103 (2002).
- [35] S. Asadabadi and H. Akbarzadeh, *Physica B: Condensed Matter* **349**, 76 (2004).
- [36] S. Jalali Asadabadi, *Phys. Rev. B* **75**, 205130 (2007).
- [37] P. Novák, K. Knížek, M. Maryško, Z. Jiráček, and J. Kuneš, *J. Phys.: Condens. Matter* **25**, 446001 (2013).
- [38] P. Novák, V. Nekvasil, and K. Knížek, *J. Magn. Magn. Mater.* **358-359**, 228 (2014).
- [39] P. Novák, J. Kuneš, and K. Knížek, *Opt. Mater.* **37**, 414 (2014).
- [40] P. Novák, K. Knížek, Z. Jiráček, and J. Buršík, *J. Magn. Magn. Mater.* **381**, 145 (2015).
- [41] T. Yoshioka, H. Tsuchiura, and P. Novák, *Materials Research Innovations* **19**, S4 (2015).
- [42] P. Veverka, O. Kaman, K. Knížek, P. Novák, M. Maryško, and Z. Jiráček, *J. Phys.: Condens. Matter* **29**, 035803 (2016).
- [43] D. Sedmidubský, V. Jakeš, K. Rubešová, P. Nekvindová, T. Hlášek, R. Yatskiv, and P. Novák, *J. Alloys Compd.* **810**, 151903 (2019).
- [44] H. P. Christensen, *Phys. Rev. B* **19**, 6564 (1979).
- [45] N. Agladze and M. Popova, *Solid State Communications* **55**, 1097 (1985).
- [46] M. N. Popova, E. P. Chukalina, B. Z. Malkin, and S. K. Saikin, *Phys. Rev. B* **61**, 7421 (2000).
- [47] P. Babkevich, A. Finco, M. Jeong, B. Dalla Piazza, I. Kovacevic, G. Klughertz, K. W. Krämer, C. Kraemer, D. T. Adroja, E. Goremychkin, T. Unruh, T. Strässle, A. Di Lieto, J. Jensen, and H. M. Rønnow, *Phys. Rev. B* **92**, 144422 (2015).
- [48] J. Magariño, J. Tuchendler, P. Beauvillain, and I. Laursen, *Phys. Rev. B* **21**, 18 (1980).
- [49] P. E. Hansen, T. Johansson, and R. Nevald, *Phys. Rev. B* **12**, 5315 (1975).
- [50] G. Matmon, S. A. Lynch, T. F. Rosenbaum, A. J. Fisher, and G. Aeppli, *Phys. Rev. B* **94**, 205132 (2016).
- [51] K. N. Gorbachenya, S. V. Kurilchik, V. E. Kisel, A. S. Yasukevich, N. V. Kuleshov, A. S. Nizamutdinov, S. L. Korableva, and V. V. Semashko, *Quantum Electronics* **46**, 95 (2016).
- [52] F. Auzel, S. Hubert, and D. Meichenin, *Appl. Phys. Lett.* **54**, 681 (1989).
- [53] D. Bitko, T. F. Rosenbaum, and G. Aeppli, *Phys. Rev. Lett.* **77**, 940 (1996).
- [54] F. Rucker and C. Pfeleiderer, *Rev. Sci. Instrum.* **90**, 073903 (2019).
- [55] P. Beauvillain, C. Chappert, J. Renard, J. Griffin, and I. Laursen, *J. Magn. Magn. Mater.* **15-18**, 421 (1980).
- [56] C. Kraemer, N. Nikseresht, J. O. Piatek, N. Tsyrlin, B. D. Piazza, K. Kiefer, B. Klemke, T. F. Rosenbaum, G. Aeppli, C. Gannarelli, K. Prokes, A. Podlesnyak, T. Strässle, L. Keller, O. Zaharko, K. W. Krämer, and H. M. Rønnow, *Science* **336**, 1416 (2012).
- [57] D. I. Abubakirov, K. Matsumoto, H. Suzuki, and M. S. Tagirov, *J. Phys.: Condens. Matter* **20**, 395223 (2008).
- [58] P. Babkevich, M. Jeong, Y. Matsumoto, I. Kovacevic, A. Finco, R. Toft-Petersen, C. Ritter, M. Månsson, S. Nakatsuji, and H. M. Rønnow, *Phys. Rev. Lett.* **116**, 197202 (2016).
- [59] I. V. Romanova, S. L. Korableva, V. I. Krotov, B. Z. Malkin, I. R. Mukhamedshin, H. Suzuki, and M. S. Tagirov, *J. Phys.: Conf. Ser.* **478**, 012026 (2013).
- [60] S. Salaün, M. T. Fornoni, A. Bulou, M. Rousseau, P. Simon, and J. Y. Gesland, *J. Phys.: Condens. Matter* **9**, 6941 (1997).
- [61] P. Beauvillain, J. Renard, and J. Magariño, *J. Magn. Magn. Mater.* **15-18**, 31 (1980).

- [62] K. Heyde, K. Binnemans, and C. Görrler-Walrand, *J. Chem. Soc., Faraday Trans.* **94**, 843 (1998).
- [63] W. L. Feng, Z. Han, and Y. C. Zhong, *Radiat. Eff. Defects Solids* **164**, 679 (2009).
- [64] J. Cheng, J. Wen, Y. Chen, M. Yin, and C. Duan, *J. Rare Earths* **34**, 1048 (2016).
- [65] S. Hüfner, *Optical Spectra of Transparent Rare Earth Compounds Academic*, Vol. 147 (Academic Press, New York, 1978).
- [66] B. Wybourne, *Spectroscopic Properties of Rare Earths* (Interscience Publishers, New York, 1965).
- [67] P. Delange, S. Biermann, T. Miyake, and L. Pourovskii, *Phys. Rev. B* **96**, 155132 (2017).
- [68] K. W. H. Stevens, *Proc. Phys. Soc. Sec. A* **65**, 209 (1952).
- [69] D. M. Ceperley and B. J. Alder, *Phys. Rev. Lett.* **45**, 566 (1980).
- [70] J. P. Perdew and Y. Wang, *Phys. Rev. B* **45**, 13244 (1992).
- [71] D. C. Langreth and J. P. Perdew, *Phys. Rev. B* **21**, 5469 (1980).
- [72] J. P. Perdew, K. Burke, and Y. Wang, *Phys. Rev. B* **54**, 16533 (1996).
- [73] J. P. Perdew, K. Burke, and M. Ernzerhof, *Phys. Rev. Lett.* **77**, 3865 (1996).
- [74] Z. Wu and R. E. Cohen, *Phys. Rev. B* **73**, 235116 (2006).
- [75] V. I. Anisimov, I. V. Solovyev, M. A. Korotin, M. T. Czyżyk, and G. A. Sawatzky, *Phys. Rev. B* **48**, 16929 (1993).
- [76] M. T. Czyżyk and G. A. Sawatzky, *Phys. Rev. B* **49**, 14211 (1994).
- [77] V. I. Anisimov, F. Aryasetiawan, and A. I. Lichtenstein, *J. Phys.: Condens. Matter* **9**, 767 (1997).
- [78] E. Sjöstedt, L. Nordström, and D. Singh, *Solid State Commun.* **114**, 15 (2000).
- [79] G. K. H. Madsen, P. Blaha, K. Schwarz, E. Sjöstedt, and L. Nordström, *Phys. Rev. B* **64**, 195134 (2001).
- [80] S. Cottenier, *Density Functional Theory and the Family of (L)APW-Methods: A Step-by-Step Introduction, 2nd ed.* (Instituut voor Kern-en Stralingsfysica, KU Leuven, Belgium, 2013), pp. 15–16.
- [81] E. Ghasemikhah, S. Jalali Asadabadi, I. Ahmad, and M. Yazdani-Kachoei, *RSC Adv.* **5**, 37592 (2015).
- [82] M. Yazdani-Kachoei, S. Jalali-Asadabadi, I. Ahmad, and K. Zarringhalam, *Sci. Rep.* **6**, 31734 (2016).
- [83] M. Yazdani-Kachoei, S. Jalali-Asadabadi, and N. Arianmehr, *Comput. Mater. Sci.* **164**, 205 (2019).
- [84] M. Yazdani-Kachoei and S. Jalali-Asadabadi, *RSC Adv.* **9**, 36182 (2019).
- [85] C. Rudowicz, *J. Phys. C* **18**, 1415 (1985).
- [86] A. Abragam and B. Bleaney, *Electron Paramagnetic Resonance of Transition Ions*, International Series of Monographs on Physics (Clarendon Press, Oxford, 1970).
- [87] C. Rudowicz and C. Y. Chung, *J. Phys.: Condens. Matter* **16**, 5825 (2004).
- [88] I. Ryabov, *J. Magn. Reson.* **140**, 141 (1999).
- [89] H. P. Christensen, *Phys. Rev. B* **17**, 4060 (1978).
- [90] I. V. Romanova, A. V. Egorov, S. L. Korableva, B. Z. Malkin, and M. S. Tagirov, *J. Phys.: Conf. Ser.* **324**, 012034 (2011).
- [91] H. P. Christensen, *Phys. Rev. B* **19**, 6573 (1979).
- [92] N. Uehara, K. ichi Ueda, and Y. Kubota, *Jpn. J. Appl. Phys.* **35**, L499 (1996).
- [93] J. E. Miller and E. J. Sharp, *J. Appl. Phys.* **41**, 4718 (1970).
- [94] A. Bensalah, Y. Guyot, M. Ito, A. Brenier, H. Sato, T. Fukuda, and G. Boulon, *Opt. Mater.* **26**, 375 (2004), third International Symposium on Lasers and Nonlinear Optical Materials (ISLNOM-3).
- [95] H. N. Dong, W. C. Zheng, and S. Y. Wu, *Phys. Status Solidi (b)* **240**, 120 (2003).
- [96] M. P. Davidova, S. B. Zhdanovich, B. N. Kazakov, S. L. Korableva, and A. L. Stolov, *Optica i spektr* **42**, 577 (1977).
- [97] H. M. Rønnow, J. Jensen, R. Parthasarathy, G. Aeppli, T. F. Rosenbaum, D. F. McMorrow, and C. Kraemer, *Phys. Rev. B* **75**, 054426 (2007).
- [98] H. P. Jenssen, A. Linz, R. P. Leavitt, C. A. Morrison, and D. E. Wortman, *Phys. Rev. B* **11**, 92 (1975).
- [99] A. Tkachuk, S. Ivanova, L. Isaenko, A. Yelisseyev, S. Payne, R. Solarz, M. Nostrand, R. Page, and S. Payne, *Acta Phys. Pol. A* **95**, 381 (1999).
- [100] S. Edvardsson and D. Åberg, *Comput. Phys. Commun.* **133**, 396 (2001).
- [101] L. Holmes, T. Johansson, and H. Guggenheim, *Solid State Commun.* **12**, 993 (1973).
- [102] L. Misiak, *Acta Phys. Pol. A* **83**, 141 (1993).
- [103] X. Xun, S. Feng, and R. Xu, *Mater. Res. Bull.* **33**, 369 (1998).
- [104] L. Misiak, P. Mikolajczak, and M. Subotowicz, *Phys. Status Solidi A* **97**, 353 (1986).
- [105] P. Atkins, M. Child, and P. C., *Tables for Group Theory* (Oxford University Press, Oxford, 2006).
- [106] P. Blaha, K. Schwarz, G. K. H. Madsen, D. Kvasnicka, J. Luitz, R. Laskowski, F. Tran, and L. D. Marks, WIEN2k: An Augmented Plane Wave + Local Orbitals Program for Calculating Crystal Properties, Technische Universität Wien, Vienna, Austria (2018), [http://wien2k.at/reg\\_user/textbooks/usersguide.pdf](http://wien2k.at/reg_user/textbooks/usersguide.pdf).
- [107] P. Blaha, K. Schwarz, F. Tran, R. Laskowski, G. K. H. Madsen, and L. D. Marks, *J. Chem. Phys.* **152**, 074101 (2020).
- [108] H. J. Monkhorst and J. D. Pack, *Phys. Rev. B* **13**, 5188 (1976).
- [109] J. Kuneš, R. Arita, P. Wissgott, A. Toschi, H. Ikeda, and K. Held, *Comput. Phys. Commun.* **181**, 1888 (2010).